DEVELOPMENT OF A MULTI-RANGE LIGHTNING CURRENT MEASUREMENT SYSTEM WITH A WIDE DYNAMIC RANGE FROM MILLI-AMPS TO HUNDREDS OF KILO-AMPS

WANG SHAOYANG

PhD

The Hong Kong Polytechnic University

2023

The Hong Kong Polytechnic University

Department of Building Environment and Energy Engineering

Development of a Multi-Range Lightning Current Measurement System with a Wide Dynamic Range from Milli-amps to Hundreds of Kilo-amps

Wang Shaoyang

A thesis submitted in partial fulfilment of the requirements for the degree of Doctor of Philosophy

August 2023

Certificate of Originality

I hereby declare that this thesis is my own work and that, to the best of my knowledge and belief, it reproduces no material previously published or written, nor material that has been accepted for the award of any other degree or diploma, except where due acknowledgement has been made in the text.

Name of Student: Wang Shaoyang

Department of Building Environment and Energy Engineering

The Hong Kong Polytechnic University

Hong Kong SAR, China

August 2023

Abstract

Measuring the lightning current in a lightning rod with a wide dynamic range is a challenge. Currently, there is a lack of suitable equipment to study the current variation in the streamer process of lightning. The existing lightning current observation equipment is mainly designed to measure the peak current generated by the stroke, with a measurement range typically from tens of amperes to hundreds of kiloamperes. While a few devices can observe leader currents of a few amperes, they are incapable of measuring corona discharges and the streamer process ranging from a few milliamps to hundreds of milliamps. This lack of observational data severely hinders the understanding of lightning initiation processes. Herein, in this thesis, we have proposed and implemented a wide dynamic range lightning current measurement and acquisition system with multi-channel active preamplifiers, which has the ability to measure lightning channel current as low as 10mA with a shock tolerance capability of 400kA. The contents in this thesis include a thorough literature review of relevant works, the framework and design principle of each subsystem of the proposed wide range current measurement system, laboratory and field test results of the system, and preliminary analyses of the field observation results using this system.

The complete wide-range current measuring system we developed consists of two large parts: hardware and software. The hardware design mainly includes input signal attenuation and protection units, a four-channel preamplifier with different optimization directions, Analog-Digital-Converters (ADC), digital signal processing, optical

communication, timing and isolated power supply. The software mainly includes the multi-channel data merging, signal triggering and buffering, Graphical-User-Interface (GUI) display, and data storage. The feasibility and successful implementation of this proposal are attributed to the commercialization of ultra-low noise op-amps and the increasing processing capability of computers. And the Shenzhen Meteorological Gradient Tower (SZMGT) also provided an excellent experimental platform for lightning currents observation. After installing this system on SZMGT, the background noise of current measurement is reduced to below 10 mA. We have successfully observed the corona discharge phenomenon with a current of several hundred milliamperes just before the occurrence of a lightning stroke, with the return stroke current exceeding 220 kA. This is the first time that lightning currents over seven orders of magnitude have been continuously observed and recorded, ranging from a few milliamperes to hundreds of kiloamperes. This observation will be beneficial in studying the physical processes in the initiation stage of lightning. Additionally, the system design has optimized its ability to resist electromagnetic interference, reduced installation space requirements, and simplified data path communication. These improvements make it more suitable for installation on SZMGT with complex electromagnetic environment.

Publications arising directly from the thesis

S. Wang and M. Chen, "Shock-Tolerated Multi-Range Low-Noise Analog Front-End for Lightning Current Measurements from Milli-amps to Hundreds of Kilo-amps," IEEE Transactions on Instrumentation & Measurement, 2023 (Under review)

S. Wang, M. Chen, Z. Qiu, H. Zhuang, Y. Gao and R. Huang, "Verification of a Sub-ampere Level Lightning Current Measuring Module with a Low Resistance Shunt on a Tall Tower under Complex Electromagnetic Environment," Measurement, 2023 (Under review)

S. Wang, M. Chen, Y. Gao, and Y.-P. Du, "Preliminary Results of Corona Discharge Current Measurements in the Early Formation of Lightning on Tower," in 2023 12th Asia-Pacific International Conference on Lightning (APL), IEEE, 2023, pp. 1–4, doi: 10.1109/APL57308.2023.10182038.

S. Wang, M. Chen, and Y. Du, "Shock Tolerated Low Noise Analog Front-End for Milliamp Measurement on a Low Resistance Shunt," in 2023 IEEE International Instrumentation and Measurement Technology Conference (I2MTC), IEEE, 2023, pp. 01–05, doi: 10.1109/I2MTC53148.2023.10175986.

S. Wang, M. Chen, and Y.-P. Du, "Rapid Building of a Low-Cost VLF Electromagnetic Field Antenna Based on Mature Printed Circuit Board Technology and Its Application," in URSI GASS 2023 XXXV th URSI General Assembly and Scientific Symposium, 2023 (Extended abstract).

S. Wang and M. Chen, "A Shock-Tolerant Multi-Range Low-Noise Lightning Current Measuring System for Currents Ranging from Milliamps to Hundreds of Kiloamps," in American Geophysical Union Fall Meeting 2023, 2023. (Abstract, Accepted)

Publications coauthored that related to this thesis

Y. Gao, M. Chen, Z. Qin, Z. Qiu, S. Wang, G. Zhang, Q. Qi and Y. Du, "Attachment Processes of Negative Flashes with Multiple Return Strokes to a Tall Tower Observed at Close Distances," Atmospheric Research, 2023 (Under review)

Y. Gao, M. Chen, Z. Qin, Z. Qiu, Y. Yang, Y. Du, S. Wang and G. Zhang, "The spatial evolution of upward positive stepped leaders initiated from a 356-m-tall tower in Southern China," Journal of Geophysical Research: Atmospheres, vol. 125, no. 2, p. e2019JD031508, 2020, doi: 10.1029/2019JD031508.

Z. Qiu, Y. Yang, Z. Qin, M. Chen, F. Lyu, H. Guo, Y. Du, Y. Gao, G. Zhang and S. Wang, "Optical and Current Measurements of Lightning Attachment to the 356-m-High Shenzhen Meteorological Gradient Tower in Southern Coastal Area of China," IEEE Access, vol. 7, pp. 155372–155380, 2019, doi: 10.1109/ACCESS.2019.2949127.

G. Zhang, M. Chen, S. Wang, Y. Gao, and Y.-P. Du, "A New FDTD Model for Lightning Return Stroke Channel Above Lossy Ground and Its Validation with Rocket-triggered Lightning Data," IEEE Access, pp. 1–1, 2023, doi: 10.1109/ACCESS.2023.3303478.

Y. Gao, M. Chen, S. Wang, Z. Qin, Z. Qiu, G. Zhang, R. Cai, J. Zhang and Y. Du, "Attachment Process of A Downward Negative Flash with Multiple Return Strokes Struck to a 356-m-Tall Tower in Southern China," in 2023 12th Asia-Pacific International Conference on Lightning (APL), IEEE, 2023, pp. 1–5, doi: 10.1109/APL57308.2023.10181905.

Projects participated

Identifications of ionospheric responses to lightning events with narrowband LF Loran-C signals as an ionospheric diagnostic, funded by the General Research Fund (RGC Ref No. 15234323) from Hong Kong Research Grants Council in 2023. The total funding for this project is HK$1,493,000, and it is scheduled to start on Jan. 1, 2024.

Development of a low-noise broadband lightning current measuring system with a wide dynamic range from milli-amperes to hundreds of kilo-amperes, funded by the General Research Fund (RGC Ref No. 15219121) from Hong Kong Research Grants Council in 2021. The total funding for this project is HK$838,000, and it is currently undergoing.

Development of ionospheric D detector based on Loran-C signal, funded by the BEEE of FCE, The Hong Kong Polytechnic University in 2020. The total funding for this project is HK$236,000, and it has already been completed.

Acknowledgements

First of all, I would like to express my sincere gratitude to my Chief Supervisor, Prof. Chen Mingli, and Prof. Du Yaping, both from the Department of Building Environment and Energy Engineering (BEEE) at The Hong Kong Polytechnic University. Their readily available supervision, invaluable suggestions, patient guidance, and continuous help not only supported me throughout my studies but also in my later career life.

I would like to express my appreciation to my group members: Dr. Tao Lu, Dr. Shuyao Cai, Dr. Yanchi Shen, Dr. Mingkit Chan, Dr. Zilong Qin, Dr. Yan Gao, Dr. Ge Zhang, and Dr. Fanchao Lyu. I feel fortunate to have worked alongside such kind and considerate colleagues. Over the past six years, we have shared countless amazing and memorable experiences. In our academic work, we conducted the lightning observation experiment in Shenzhen, observed many meaningful flash cases that occurred at the top of the Shenzhen Tower, and accomplished some interesting research work together. I treasure the friendships with them and sincerely wish all of them a bright future.

To study the initiation process of upward flashes on SZMGT, our research group established a lightning observation site 440 meters away from the tower base. I am grateful for the support and assistance provided by the Shenzhen Meteorological Services Center, without which I could not have successfully conducted the observation experiment and obtained the necessary data to complete my PhD thesis. I would like to express my gratitude to Mr. Zongxu Qiu, Mr. Hongbo Zhuang, and Mr. Hongbo Guo from the Shenzhen Meteorological Services Center, as well as Mr. Runquan Huang from Shenzhen City Ouxintai Science and Technology Co., Ltd.

To study the ionosphere responses to lightning events, we also set up receiving equipment on the rooftop in the campus of the University of Science and Technology of China in Hefei, China. We successfully received Loran-C skywave and groundwave signals that can be used to invert ionospheric disturbances. I am grateful for the support and assistance provided by USTC, and would also like to express my gratitude to my undergraduate supervisor, Prof. Baoyou Zhu, and my former group member, Dr. Feifan Liu.

Last but not least, I would like to express my deepest gratitude to my grandfather and all other family members. I could not have completed this work without their love and continuous support throughout my life.

Table of Contents

List of Figures

List of Tables

List of Abbreviations

ADC	Analog-to-Digital Converter
AFE	Analog Front-End
BJT	Bipolar Junction Transistor
BW	Bandwidth
CG	Cloud-to-Ground
CMOS	Complementary Metal Oxide Semiconductor
CMRR	Common Mode Rejection Ratio
CVR	Current-Viewing Resistor
DAC	Digital-to-Analog Converter
DAQ	Data Acquisition
D-MOSFET	Depletion mode Metal Oxide Semiconductor Field Effect Transistor
DNL	Downward Negative Leader
E-MOSFET	Enhancement mode Metal Oxide Semiconductor Field Effect Transistor
E/O	Electric-to-Optical Converter
EMI	Electromagnetic Interference
FPGA	Field Programmable Gate Arrays
GDT	Gas Discharge Tube
GUI	Graphical User Interface
INA	Instrumentation Amplifier
JFET	Junction Field Effect Transistor
LDO	Low-Dropout Regulator

LNA	Low-Noise Amplifiers
MAC	Media Access Control Address
MOSFET	Metal Oxide Semiconductor Field Effect Transistor
MOV	Metal Oxide Varistor
O/E	Optical-to-Electric Converter
RS	Return Stroke
SOC	System on Chip
SNR	Signal-to-Noise Ratio
SPD	Surge Protective Device
SZMGT	Shenzhen Meteorological Gradient Tower
THD	Total Harmonic Distortion
TVS	Transient Voltage Suppression
UPL	Upward Positive Leader
VND	Voltage Noise Density

Chapter 1. Introduction

Lightning is a high-energy electrical discharge phenomenon in nature, which usually occurs within or between clouds during thunderstorms. When the lightning channel extends from the cloud and connected to the ground, the cloud-to-ground (CG) lightning is formed, and usually cause serious damages such as wildfires, power outages, structure and electronic device damage, and even casualties. According to the statistics of optical satellites in recent years, an average of 44 lightning strikes occurs every second globally. Most of them occur in low and middle latitudes, and a few also occur in polar regions (Christian, 2003). Due to its strong current, high temperature, strong electromagnetic radiation, and violent shock waves, lightning can instantly cause huge destructive effects, resulting in lightning disasters. (Uman et al., 1964). According to reports in Canada, fires caused by lightning account for 85% of the total burned area and 35% of the reported fires (Weber & Stocks, 1998). Additionally, lightning has a significant impact on construction, communication, power transmission, the electronic industry, and human life safety. However, the occurrence of lightning in nature cannot be controlled or prevented by human beings. Therefore, the study of the physical characteristics of lightning discharge is essential in order to minimize its harm and achieve effective lightning protection.

While scientists continue to study the intricacies of how thunderstorm clouds charge, there are some fundamental concepts regarding the electrification of thunderstorms that have been widely accepted. One such concept is the transfer of ions between colliding particles, which can lead to electrification through the triboelectric effect. Benjamin Franklin's famous kite experiment in 1752 provided early evidence that lightning is indeed an electrical phenomenon. By the late 19th century, advancements in spectroscopy and photography allowed researches to observe the optical phenomena of lightning (Igoe, 2016). Later, in the mid-20th century, the rapid growth of electronic technology led to the first measurement of lightning current waveforms in Russia using tethered balloons (Stekolnikov & Valeev, 1937). To this day, studying the lightning current as well as the electromagnetic field it generates remains crucial for lightning research.

1.1. About Upward Lightning Leader

Through the analysis of a large number of lightning data, four different types of lightning discharges are classified according to the polarity of the charge effectively transferred to the ground and the propagation direction of the initial leader. Among these four types, downward negative lightning discharges make up 90% of all CG lightning (Rakov & Uman, 2003). These discharges occur when a downward-moving leader extends from the cloud and delivers a negative charge to the ground. The development of downward negative lightning can be divided into several stages, including cloud charge distribution, initial breakdown, stepped leader, attachment process, first return stroke, and subsequent strokes (Pierce, 1955; Uman, 2001). Among these stages, the upward positive leader plays a crucial role in the selection of the grounding point, making it a key focus in lightning physics and protection research.

The phenomenon known as upward lightning, or upward leader, is typically initiated by tall ground-based objects, such as mountain-top towers and tall buildings. It is commonly believed that when a building is below 100m in height, only downward lightning strikes occur, whereas buildings taller than 500m, only upward lightning occurs (Rakov, 2003; Rakov & Uman, 2003). Moreover, the concept of an "effective height" is used when evaluating buildings situated on mountains (Pierce, 1972; Golde, 1978; Zhou et al., 2009). As urban buildings continue to grow taller, the importance of effective lightning monitoring, early warning, and preventive measures increases. However, all of this relies on a fundamental understanding of the physical mechanism behind lightning. In the past decade, considerable attention has been devoted to studying the properties of lightning leaders. Nevertheless, due to limitations in measurement technology, our knowledge of the occurrence of the upward leader just before a lightning stroke remains quite limited.

1.2. Lightning Current Measurement

In order to observe the discharge process of the lightning more conveniently, the method of manually triggering lightning by extending a thin wire (either grounded or ungrounded) from a small rocket into the gap between the ground and a charged cloud overhead was first proposed in 1961 (Brook et al., 1961), and was successfully implemented at sea in 1967 (Newman et al., 1967). Artificially triggered lightning offers a discharge process similar to natural lightning, with known occurrence time and location, making it advantageous for easy observation of discharge parameters. As a result, it is widely used in the field of lightning research. However, when using a slow or stationary conductor to trigger a discharge, a higher background electric field is required due to the electric field shielding effect caused by corona discharge. This effect has a greater impact on the research of the upward leader process on structures (Brook et al., 1961). In this case, the observation of lightning phenomena on tall buildings serves as an important supplement.

In both mentioned approaches, either Rogowski coils or low-resistance current-viewing resistors (CVR, also known as low-resistance-current shunts) were used to measure the lightning channel currents (J. Takami & S. Okabe, 2007; Z. Qiu et al., 2019). These current measurement devices typically focused on measuring large currents ranging from several to hundreds of kiloamperes (Gruchalla, 2008; Z. Li et al., 2011). To measure the initial upward leaders current, low-range current sensors were employed to reduce the noise level to several amperes (Visacro et al., 2017). Some smaller-range current detection devices were also used to measure the current on the lightning rod, but encountered issues such as saturation and fuse blowing (Moore et al., 2000). On the other hand, modeling studies suggest that the current of the corona discharge phenomenon in the lightning initiation process was less than several milliamperes (Aleksandrov et al., 2005; Bazelyan et al., 2008). Additionally, experiments of corona discharge at a sharp tip under thunderstorms revealed that the current was in the range of a few to tens of microamperes (D'Alessandro, 2009). It is important to note that all current measurement devices can be categorized into two groups: those for detecting large return stroke currents after the lightning leader initiations, which lack the ability to capture small current events, and those for measuring small current events such as corona discharges before the lightning leader initiation, which are not enable to withstand high current shocks. Consequently, there exists a big gap in understanding the transition process from corona discharge to leader development due to the lack of a full-range lightning current measuring device.

1.3. Main Contributions in This Research Work

As mentioned above, the existing lightning current measurement technology is insufficient to meet the requirements for further research on the lightning leader process. This study aims to develop a comprehensive current acquisition system with a wide dynamic range, specifically designed for extreme electromagnetic environments encountered during lightning observation, such as high voltage and strong electromagnetic fields. Additionally, the compact and low-power design of this system allows for easy use in field experimental environments. The lightning current acquisition system primarily consists of a multi-range low-noise preamplifier unit, an analog-to-digital conversion processing unit, an optical fiber transmission and link combining unit, a timing system and computer software. Due to the specific use environment and the need for reliable field testing, most of the components cannot be built using existing commercial products. This work will involve hardware design and programming of SoC (System on Chip), FPGA (Field-Programmable Gate Array), and the host computer.

This lightning current acquisition system has the following basic specifications: measurement range from 10mA to 400kA, with a maximum analog bandwidth of 20MHz for currents over 400A. For currents below 5A, the system offers a maximum bandwidth of 3MHz, which can be adjusted based on the specific background noise at the test site. Notably, when the bandwidth is limited to 400kHz, the system's lowest range exhibits a background noise of only 4.5mArms, making it exceptionally advantageous for studying the occurrence and development of lightning upward leaders.

1.4. Outline of This Thesis

This thesis consists of eight chapters, and the organization of this thesis is described as follows:

Chapter 1 provides an introduction to the research background of this study. It outlines the research objectives, significance, and contributions. The background information discusses the mechanisms, research progress, and application value of the lightning upward leader, as well as the current research bottlenecks. Following the analysis of this background information, the research gap is identified, and the research directions and targets are presented.

Chapter 2 serves as the literature review, where the current research progress on lightning upward leaders, measurement methods for lightning channel currents, and techniques related to low-noise amplifiers are introduced. This chapter will provide a more detailed explanation of the topics mentioned in the introduction.

Chapter 3 provides a detailed overview of the lightning current acquisition system framework. It covers the specific implementation scheme for the analog front-end unit, sampling unit, laboratory tests, and field experiments. Additionally, this chapter also introduces the environment and infrastructure of the Shenzhen Meteorological Gradient Tower (SZMGT), which serves as the site for the field test.

Chapter 4 primarily discusses the hardware design of the analog front-end, and presents the preliminary test results, which demonstrate the feasibility of measuring lightning current across a wide dynamic range using a single low-resistance shunt. Additionally, this chapter mentions and compares the existing solutions to illustrate their limitations and the improvements made in this research.

Chapter 5 discusses the construction method of the acquisition system, which involves merging data from multiple channels and utilizing precise timing technology.

Additionally, this chapter will cover the hardware design of the acquisition system and provide a thorough analysis of the power supply and ground loops.

Chapter 6 provides a detailed explanation of the hardware assembly process and conducts performance tests on two crucial components of the current acquisition system: the analog front end and the optical communication link.

Chapter 7 provides a detailed description of the preliminary observation results obtained from field site. It also highlights the measures taken to address challenging electromagnetic interference, including hardware adjustments and optimizing the data processing flow.

Chapter 8 summarizes the progress made in constructing the wide range lightning current acquisition system and presents preliminary observation results. It also outlines the future plans for this project.

At the end of the report, all the references are attached.

Chapter 2. Literature Review

The subject of this study is a lightning channel current measurement and acquisition system. According to the focus of this study, this chapter will conduct a comprehensive literature review. At the beginning of this chapter, the physical process of the lightning upward leader will be explained, and it is also the starting point of this study. Secondly, the previous observations and the techniques used will be presented in detail, which will serve as the design reference and application requirements for this study. After that, considering that the focus of this study is to observe the weak current in the initial stage of lightning, the role of low-noise amplification technology is also very important, so the related technical development and achievements will also be introduced. Finally, the shortcomings of the current lightning current measurement technology will be summarized, and the feasibility of this study will be judged.

2.1. The Physical Process and the Previous Observed Results of Lightning

2.1.1. Corona Discharge and Streamer Process

Corona discharge is a typical form of partial discharge, usually caused by the ionization of fluids such as air around a conductor with high voltage. A corona occurs where the electric field strength around a conductor exceeds the dielectric strength and allows the electric charge to continuously leak from the conductor into the air (Warner

& Kunz, 1919). Usually 130V/m fair-weather electric field is not enough to generate corona discharges on grounded structures, however when thunderstorm clouds form, the atmospheric background electric field can reach ~10^4 V/m (Burke & Few, 1978). When the background electric field reaches 20kV/m, a voltage drop of about 400kV can be formed near the tip of a 20m rod, which is sufficient to form a branch of cathode-directed streamers (Aleksandrov et al., 2005).

Corona discharges also play an important role in the development of lightning channel. In laboratory simulations, it can be observed that the leader starts with a corona pulse, which is a bunch of streamers with a common stem, and then the leader channel begins to develop (Waters, 1977). Moore et al. also measured weak current pulses on the lightning rod 300 – 400 ms before the lightning strike (Moore et al., 2000).

Before the development of streamers, the role of the corona was to stabilization the electric field at the tip of the conductor. However, as the background electric field changes and the ions drift in the outer region, the corona at the tip of the conductor will continuously generate ions in order to maintain dynamic equilibrium, which also form an electric current inside the conductor (Loeb, 2022; Raizer & Allen, 1991). In 1967, Berger observed 2 – 4 mA peak corona discharges during thunderstorms on two 70m towers using the mA-meter (Berger, 1967). Aleksandrov et al. numerically simulated that the corona current of a rod with a height of 50 m is about 130 uA when the thundercloud field linearly increased to 20 kV/m over 10 s. They also shown that the corona current increased from 0.1 uA to 30 mA in 15 ms when the downward leader propagates (Aleksandrov et al., 2005). Bazelyan et al. gave the corona current peaks of 50 uA and 275 uA for rods with heights of 30m and 100m when the background electric field was 20 kV/m, respectively (Bazelyan et al., 2008). And for the streamer current, Gallimberti et al. estimated that the transform current from streamer to leader is less than 1 A based on laboratory results (Gallimberti, 1979). Gao et al. simulated the peak value of streamer discharge current at ~50 mA (Gao et al., 2000).

2.1.2. Leader Process

The lightning leader plays an important role in the process of forming the discharge channel under the strong background electric field, which can be divided into positive leader and negative leader according to the polarity of the accumulated charge on the leader head (Bruce & Golde, 1941; Pierce, 1955). The early exploration of the characteristics and mechanism of leader transport was mainly achieved by optical imaging or electromagnetic detection of long-gap discharges in the laboratory and natural downward leaders (Loeb, 1966; Krider & Radda, 1975; Krider et al., 1977).

For the negative leader, it is usually developed and transmitted in a step pattern to break down the air, which is intermittent pauses and jumps forward at a certain period of time. Schonland et al. first used a Boys camera with a temporal resolution of 0.6 microseconds to capture a negative leader step length of 10 – 200 m, a step interval of

40 – 100 μs, and a two-dimensional development speed of 3.8 × 10^5 m/s (Schonland et al., 1935). In addition, by using a fast moving film camera with the speed of 27 m/s, Berger captured a negative leader step length of 3 – 17 m, a step interval of 29 – 47 μs, and a two-dimensional development speed of 0.9 × 10^5 – 4.4 × 10^5 m/s (Berger, 1967). Based on the laboratory spark discharge, Gorin et al divided the negative step leader process into three stages: 1) A relatively dim space stem appears in the streamer area of the leader head, which develops into a bright and luminous space leader through the heating of the current, as shown in **Figure 2-1**(I); 2) The spatial leader develops bidirectionally (**Figure 2-1**(II)), its negative polarity end extends forward, while the positive polarity end develops backwards close to the leader's head (**Figure 2-1**(III)); 3) The rear end of the bidirectional leader is connected with the leader head to complete a step jump, the channel is extended instantaneously, the negative end of the bidirectional leader becomes the new head of the leader, and the leader stops immediately and enters the next step cycle (**Figure 2-1**(IV)) (Gorin et al., 1976). However, considering the differences in discharge scale and intensity between spark discharges and natural lightning, whether the negative step leader mechanism revealed in the laboratory is applicable to natural lightning has not been very sure.

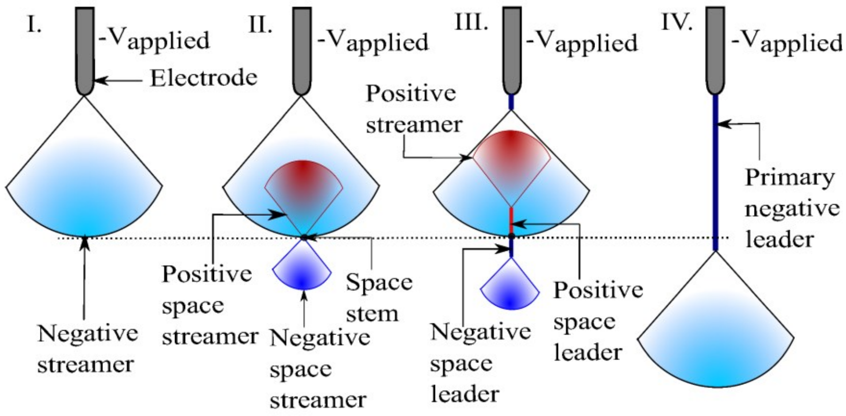

Figure 2-1. Schematic representation of stages of negative leader discharge (Das & Kumar, 2022).

For the positive leader, due to the low incidence of natural positive cloud-to-ground lightning, and the weaker light and radiation intensity emitted by positive leaders, the present research on positive leaders is significantly less than that on negative leaders (Kong et al., 2008). Berger and Vogelsanger used a Boys camera to study natural lightning occurring on high towers and found that the upward positive leader transmission speed increases with height, from an initial order of 10^4 m/s to 10^6 m/s at a height of several kilometers, and the transmission develops in a continuous pattern, with few distinct steps. (Berger & Vogelsanger, 1969). By measuring the current of classical artificially triggered lightning, Lalande et al. found that the upward positive leader starts at the top of the wire and is marked by continuous current pulses ranging from tens to hundreds of amperes at intervals of 20 – 25 μs, and the development is not continuous (Lalande et al., 1998). Through high-speed camera and synchronous measurement of the lightning channel current and electric field, Biagi et al. observed the luminous channel corresponding to the precursor current pulse that appeared before the continuous development of the upward positive leader, and obtained that the development speed of the upward positive leader within the first 100 m is 5.6×10^4 m/s (Biagi et al., 2009). Using the similar observation method, Jiang et al. found that when a rocket-triggered lightning upward positive leader developed continuously, the luminous intensity at the top of the leader is stronger than the luminous intensity of the channel behind it, and the average value of the peak value, rising edge, half-peak width, duration, transfer charge and interval time of the current pulse are 45.0 A, 0.49 μs, 0.99 μs, 3.2 μs, 4.8 μC and 19.9 μs, respectively (Jiang et al., 2013).

2.1.3. Return Stroke

Typically, the return stroke can be divided into first return stroke and the subsequent return stroke. The first return stroke occurs after the attachment process, which is the first connection between the leader developing downwards within the cloud and the leader developing upwards from the ground. After the current of first return stroke drops, if there is still a large amount of charge in the cloud, the subsequent stroke will start again after tens of milliseconds. Since the lightning current develops to the maximum value in the return stroke process, and directly determines the maximum intensity of electromagnetic radiation, the stroke current waveform and its parameter characteristics are the important basis for lightning protection design.

According to the statistics of the observation results of natural lightning and artificial lightning, most of the return stroke currents are around 10 kA, a few can reach 100 kA (Berger, 1975; Fisher et al., 1993; Visacro et al., 2004; Chowdhuri et al., 2005; Diendorfer et al., 2009), and there are very few reports exceeding 500 kA (Le Boulch & Plantier, 1990). In addition, the rise time, the maximum slope, the duration and the stroke interval of the stroke current are 0.2 – 18 μs, 5.5 – 120 kA/μs, 6.5 – 200 μs, and 31 – 900 ms, respectively.

2.2. Lightning Current Measurement Method

2.2.1. Artificial Triggered Lightning

Electric current is the source of radiation effects such as light, sound, and heat during lightning discharge, so the lightning current is one of the most important parameters in the study of lightning physical mechanism and lightning protection. However, it is very difficult to obtain current measurement data from natural discharge phenomena due to randomness. Researchers typically mount current measuring devices on the tops of tall buildings or towers, as well as on vertical wires pulled by rockets. **Table 2-1** lists tall buildings used for lightning observation internationally, and **Figure 2-2** lists the experimental sites of rocket-triggered lightning in recent years.

Table 2-1. Tall buildings used for lightning observation (Sort by country name).

Building name	Location	Height	References
Gaisberg Tower	Salzburg, Austria	100 m	(Diendorfer et al., 2009, 2011)
Morro do Cachimbo Station	Brazil	60 m	(Visacro et al., 2004, 2012)
Canadian National Tower (CN Tower)	Toronto, Canada	553 m	(Janischewskyj et al., 1997; Hussein et al., 2004)
Shenzhen Meteorological Gradient Tower (SZMGT)	Shenzhen, China	356 m	(Y. Yang et al., 2018; Z. Qiu et al., 2019)
Peissenberg Tower	Munich, Germany	160 m	(Heidler et al., 2014)
Two Italian Masts	Sasso di Pale, Italy	40 m	(Dellera et al., 1985)
Fukui Chimney	Fukui, Japan	200 m	(Wada et al., 2004; Miki et al., 2014)
Meteorological Observation Tower	Maki, Japan	150 m	(Narita et al., 1989)
Windmill and its protection tower	Uchinada, Japan	100 m 105 m	(D. Wang et al., 2008; Wu et al., 2017; X. Wang et al., 2021)
Ostankino TV Tower	Ostankino, Moscow	540 m	(Gorin, 1984)
CSIR lightning research mast	Pretoria, South Africa	60 m	(Gijben, 2012)
St. Chrischona Tower	Basel, Switzerland	250 m	(Manoochehrnia et al., 2008)
Two Lightning Tower	Mount San Salvatore, Switzerland	70 m	(Berger, 1967; Berger & Vogelsanger, 1969)
Säntis Tower	Säntis Mountain, Switzerland	124 m	(Romero et al., 2012, 2013)
Empire State Building	New York City, USA	410 m	(McEachron, 1938, 1941)

Table 2-2. Experiment for rocket-triggered lightning (Sort by start year).

Start Year	Location	References
1966	St. Petersburg, Florida, USA	(Newman et al., 1967)
1973	Massif Central, France	(Fieux et al., 1975, 1978)
1977	Aichi Prefecture et al., Japan	(Horii, 1982)
1984	Langmuir Laboratory, New Mexico, USA	(Idone & Orville, 1984; Idone et al., 1984)
1990	Florida and Alabama, USA	(Fisher et al., 1993)
1997	International Center for Lightning Research and Testing (ICLRT) at Camp Blanding, Florida.	(Rakov et al., 2002; Bejleri et al., 2004)
2005	Binzhou, Shandong, China	(Qie et al., 2007; J. Yang et al., 2008)
2006	Conghua, Guangdong, China	(Zhang et al., 2014, 2016, 2017)

2.2.2. Low Resistance Current Shunt and Current Transformer

Low-resistance coaxial shunts and current transformers such as Rogowski coils have high bandwidth, wide range, and will not interfere with the development of lightning channels due to their low impedance. And in order to obtain a larger dynamic range, two channels of different ranges will be installed. The shunts have high bandwidth, starting at DC and extending to hundreds of megahertz, the maximum current limit is usually related to size and thermal capacity, and is highly resistant to overloading (Gruchalla, 2008). However, the shunt needs to be connected in series with the rods and directly connected to the lightning channel. During the signal acquisition process, electrical isolation is required to ensure the safety of the acquisition equipment and personnel. Current transformers use magnetic fields to transmit current signals, which inherently offer the advantage of electrical isolation, but typically have a narrow bandwidth and cannot measure the DC component. Currently, Rogowski Coil can measure up to 400kA current with bandwidth from 2 kHz to 2 MHz (Z. Li et al., 2011).

Table 2-3. Current measurement equipment summary.

Site	Current Measuring Device	Recorder	Measurement Limits	Sampling Rate (MHz)	Reference
Binzhou	Shunt, 1 mΩ Two Coils.	8-channel oscilloscope	100 kA; 2 kA, 100 kA	1	(Qie et al., 2007)
Conghua	Shunt, 6.7 mΩ	Yokogawa DL850	2 kA 50 kA	5	(Zhang et al., 2014)
Shenzhen	Shunt, 0.25 mΩ	HBM GEN7tA	200 kA	10	(Y. Yang et al., 2018)
Fukui chimney	Shunt, 10 mΩ, 2 mΩ	ALCS	200 A – 13 kA 500 A – 150 kA	5	(Miki et al., 2005)
Gaisberg tower	Shunt, 0.25 mΩ	National Instruments PCI-5102	17 A – 2 kA, 330 A – 40 kA	15	(Diendorfer et al., 2009)
ICLRT	Shunt, 1 mΩ	Digitized	20 A – 2 kA	≥ 0.25	(Miki et al., 2005)
Peissenberg tower	Pearson Coil: 0.15 Hz – 200 kHz	LeCroy 9310AL	16 A – 2 kA, 156 A – 40 kA	1	(Heidler et al., 2014)
Morro do Cachimbo Station	two Pearson coils	8-channel digitizer	5A – 9 kA, 72A – 200 kA	60	(Visacro et al., 2017)

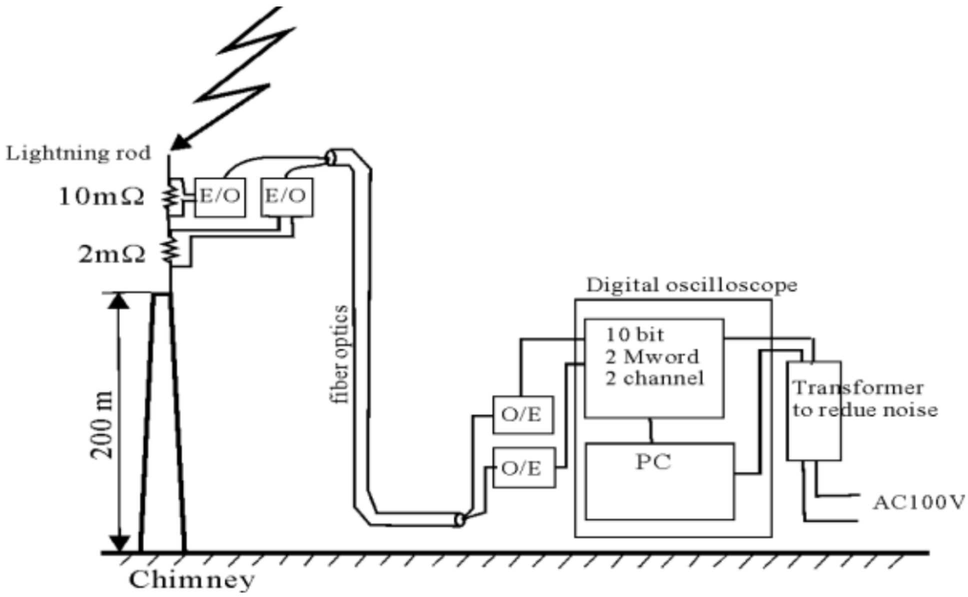

Figure 2-2. Current measurement system at Fukui Chimney Observation Site (Miki et al., 2014).

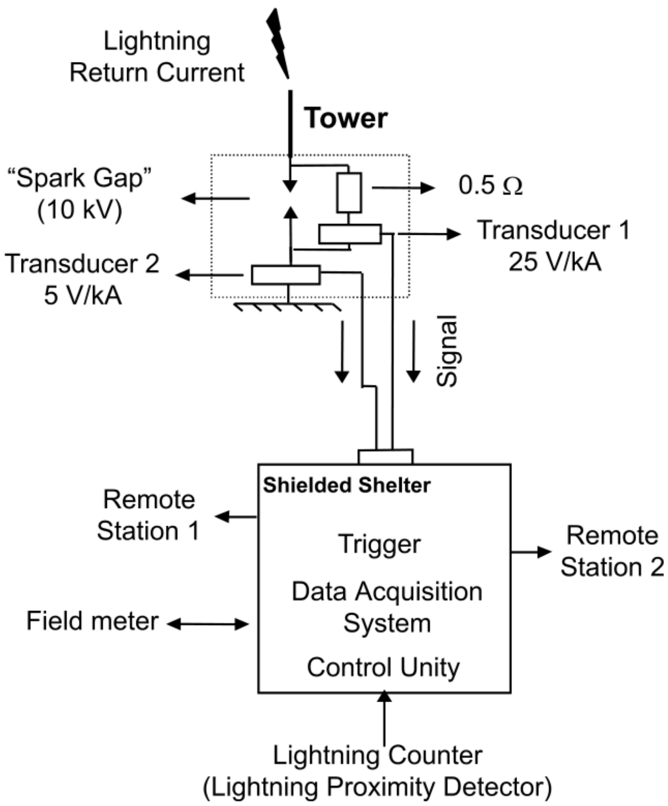

Figure 2-3. Detail of current distribution between transducers, installed under 60 m high instrumented tower at Morro do Cachimbo Station (Visacro et al., 2004).

Table 2-3 presents a summary of equipment information from different sites. It can be seen that most sites use shunts for measuring lightning current, with a current measurement upper limit of 40 – 200 kA and a sampling frequency range of 1 – 60 MSps. **Figure 2-2** and **Figure 2-3** show the current measurement systems of Fukui chimney and Morro do Cachimbo Station, respectively.

2.2.3. μA and mA Current Meter

Devices for measuring corona current are generally designed individually, and typically use a high-resistance voltage divider in conjunction with a high input impedance op-amp (D'Alessandro, 2009). Sometimes a mA meter can also be mounted on a rod with a high current shunt, but it needs to use a separating gap and make it break down in the event of lightning,

Figure 2-4 shows this configuration (Berger, 1967). Or install a fuse in front of the mA-meter and blow it when lightning strikes (Moore et al., 2000). In addition, for a larger dynamic range of current measurement, Marlton et al. measured atmospheric point discharge currents using a logarithmic current amplifier with an input range of 1pA to 10μA (Marlton et al., 2013).

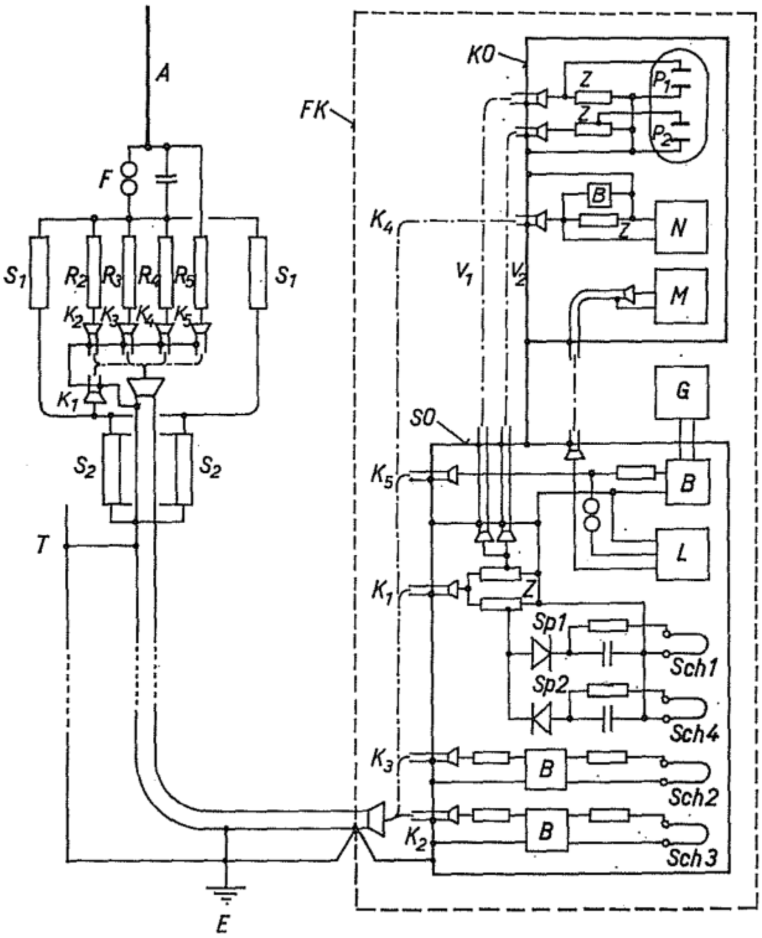

A	lightning rod or needle
B	voltage limiting devices
E	grounding system
F	tripping gap for the oscillographs, and separating gap to enable permanent registration of small corona currents at the tower.
G	corona registration mA-meter
FK	Faraday-cage
K	measuring cables
KO	cathode ray oscillograph (c.r.o.)
L	galvanometer lamp
M	tripping device for low-speed c.r.o.
N	tripping device for high-speed c.r.o.
P_1P_2	measuring plates 65 and 200 kA
R	resistors
S_1	lightning current shunt 0.8 Ω (tower 1) and 0.56 Ω (tower 2)
S_2	lightning current shunt 0.05 Ω, response-time 16 nanosec.
Sch	galvanometers
Sp	storage capacities for ±current-peak measurement
T	tower structure
V	delay cables
Z	matching resistors

Figure 2-4. Circuit diagram for current measurement on each tower located in Mount San Salvatore, Switzerland (Berger, 1967).

2.3. Low Noise AFE Design

2.3.1. Low-Noise Input Protection Techniques

In a previous study of the inception of lightning current, a spark gap technique was used as a switch for measuring both the small corona discharge current and the large return stroke current (Berger, 1967). Nonetheless, this method with a high operating voltage and non-continuity will cause a series of negative effects on the high-speed lightning current measurement, and the physical process of the lightning channel development will also be affected. In the present case, a set of input protection circuit is needed to protect semiconductor devices operating at a low voltage, and ensure the continuity of grounding impedance changes.

Generally, the input protection circuit is formed by two parts: a series current limiting circuit and a parallel voltage clamping circuit. As the voltage clamping circuit is normally off and has little contribution on the system noise floor, it can be easily constructed by using a pair of high-speed switching diodes (**Figure 2-5a**) or connecting through a pair of diodes to biased Transient-Voltage-Suppression (TVS) diodes (**Figure 2-5b**) to reduce the negative effect of the large TVS junction capacitance on the circuit bandwidth. Other Surge Protective Devices (SPDs) such as Gas Discharge Tubes (GDTs) and Metal-Oxide Varistors (MOVs) are not suitable for the present application due to their higher protection voltage.

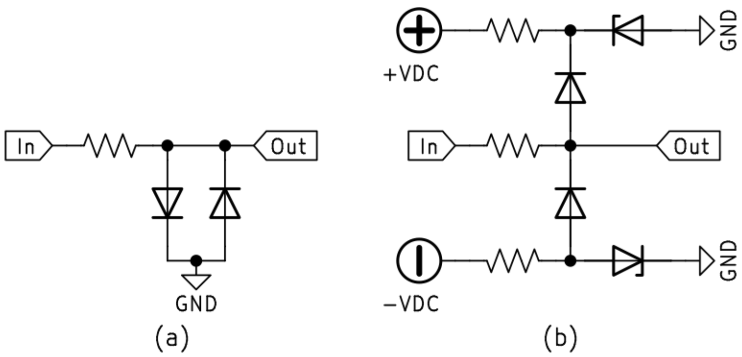

Figure 2-5. Clamping diode protection circuits, where (a) clamps the voltage to hundreds of millivolts, and (b) clamps the voltage to biased TVS voltages.

Unlike the parallel components in protection circuit, which remains in an off-state under normal conditions and generates minimal current noise, the series components contribute most of the voltage noise. And the thermal noise caused by series resistors will be an important source of noise in broadband measurements. To avoid higher thermal noise generated by larger protection resistors, some other current limiter circuits using semiconductor devices were proposed.

Figure 2-6 shows current limiter circuits constructed using JFETs, where (a), (b) and (c) are input protection circuits in ADA4177 (Analog Devices Incorporated, 2018), INA118 (Texas Instruments Incorporated, 2022) and INA818 (Texas Instruments Incorporated, 2019), respectively, and (d) is from the patent (Day & Holte, 1971). These circuits usually use JFET devices with a low drain-source saturation current (I_{DSS}) to provide a lower limit current. But they are also limited by the lower drain-source breakdown voltage (BV_{DSS}) and higher drain-source on resistance ($r_{DS(on)}$) of JFETs, which will limit the maximum operating voltage (usually not higher than 40V) and increase the thermal noise generated in the resistive channel (Schröder & Weinhausen, 1979). Since the trade-off between BV_{DSS} and $r_{DS(on)}$ of JFET is limited by the semiconductor material, which is known as the "silicon limit" (Hu, 1979), other materials such as SiC can be used to increase the protection voltage while reducing the thermal noise generated by the channel resistance, but few manufacturers can produce it.

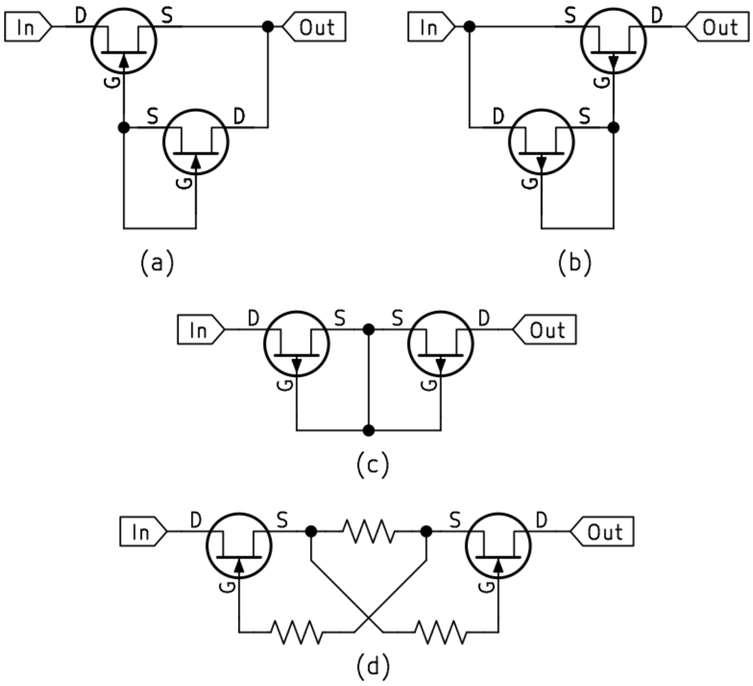

Figure 2-6. Current limiter circuits with JFETs.

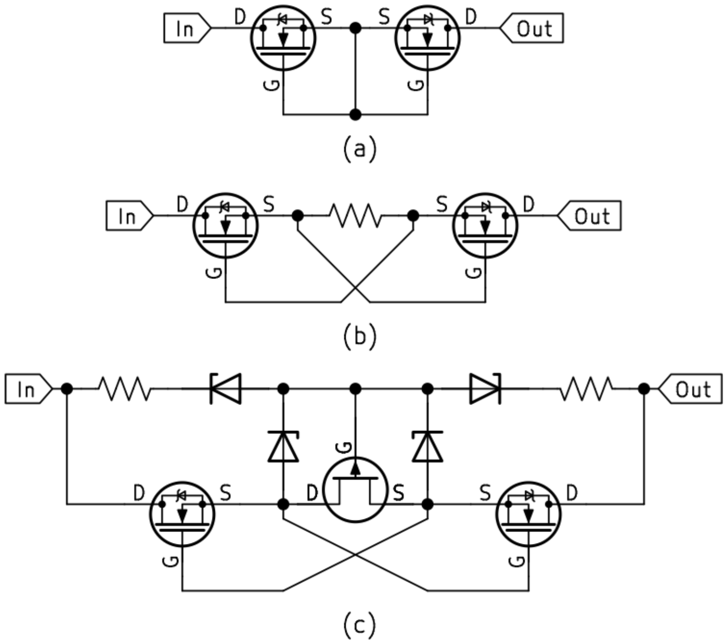

Figure 2-7. Current limiter circuits with D-MOSFETs.

Another alternative is to use n-channel D-MOSFETs instead of JFETs, which have similar characteristics under negative gate-source bias with higher BV_{DSS} and lower $r_{DS(on)}$. **Figure 2-7** shows current limiter circuits constructed using D-MOSFETs. Where (a) is a basic circuit using the I_{DSS} characteristic of D-MOSFET. (b) is a circuit with a resistor added to that in (a) to generate a negative gate-source bias when current flows, which can decrease the limit current further (Apex Microtechnology, 2017). And (c) a circuit with a p-channel JFET instead of the resistor in (b) to further drop-off the protection current after the voltage exceeding the threshold (Lei & Calif, 1998). Besides, the more common enhancement mode metal oxide semiconductor field effect transistor (E-MOSFET) can also be used for current limiting with an independent voltage bias or gate driver (Yun et al., 1995), but the circuit is much more complicated and not suitable for low-noise front-end circuits.

2.3.2. Low-Noise Amplifier Techniques

There are several techniques that can reduce referred-to-input (RTI) voltage noise to a nano-volt level. They can be broadly classified into two categories: chopper amplifiers and precision amplifiers. Chopper amplifiers use modulation methods to minimize low-frequency voltage noise and DC offsets in op amps, and an RTI voltage noise of 0.73 $\mathrm{nV}/\sqrt{\mathrm{Hz}}$ was achieved in previous study (Drung & Storm, 2011). Since AC signals are amplified in chopper amplifiers, transformers with higher transformation turn ratio can be used to further reduce the voltage noise to 0.55 $\mathrm{nV}/\sqrt{\mathrm{Hz}}$ (Harris & Smith, 1957; Z. Wang et al., 2014). Benefiting from the lower corner of $1/f$ noise, chopper amplifiers can provide good low-frequency noise performance (J. Li et al., 2020), but their bandwidth is limited due to the limitation of the modulation frequency, making it unsuitable for broadband applications.

Non-chopper precision amplifiers can also achieve a nano-volt noise level in broadband with the input stage made of low-noise Bipolar Junction Transistor (BJT), Junction Field Effect Transistor (JFET) or Complementary Metal-Oxide Semiconductor (CMOS) components (Leach, 1994). The specific manufacturing process has a great influence on the noise performance. In general, BJTs have a lower input voltage noise with a larger bias current, while JFETs and CMOS have a lower input current noise with a higher input resistance (Moghimi, 2010). Super-beta transistors are alternative ones to traditional BJTs, which can reduce input bias current with a current gain of 1,000 to 10,000 at a collector current level as low as 1 μA (Au, 1972). With this technology, a voltage noise of 0.8 $\mathrm{nV}/\sqrt{\mathrm{Hz}}$ is available through THAT 300 Series matched BJT array (THAT Corporation, 2013), and 1 $\mathrm{nV}/\sqrt{\mathrm{Hz}}$ is achievable by the INA849 monolithic instrumentation amplifier (INA) chip with a maximum bias current of 20 nA (Texas Instruments Incorporated, 2021). Besides, the voltage noise of JFET and CMOS can also be reduced by increasing the geometry of transistors, but the input capacitance will increase at the same time (Levinzon & Vandamme, 2011). The IF3602 produced by InerFET Corporation has achieved a voltage noise of 0.35 $\mathrm{nV}/\sqrt{\mathrm{Hz}}$ by itself, and 0.6 $\mathrm{nV}/\sqrt{\mathrm{Hz}}$ in application where other factors are considered (S. Wang et al., 2022), but its input capacitance is as large as 650 pF (InterFET Corporation, 2022). In contrast, the IF9030 is a more balanced product, which offers a voltage noise of 0.5 $\mathrm{nV}/\sqrt{\mathrm{Hz}}$ (Levinzon, 2005), and a maximum input capacitance of 60 pF (InterFET Corporation, 2019).

Considering the rapid changes in the electric field near the lightning channel, the instrumentation amplifiers (INA) with high common-mode rejection ratio (CMRR) are selected. An INA can be built using three op amps, four ratio-matched resistors, and a gain-setting resistor, or a single INA chip that is integrated and optimized by the manufacturer. Usually the integrated INA has a higher CMRR due to the use of laser trimming technology to complete the resistance ratio matching inside the chip, which is also easier to use (Kitchin & Counts, 2006). However, this type of chip has limited choices and is usually aimed at industrial applications with low bandwidth. **Table 2-4** shows the summarized specifications of the latest generation integrated INAs which provide the bandwidth of at least close to 1MHz with very low equivalent reference to input (RTI) noise.

Table 2-4. The specification summarization of latest generation integrated INA (Bandwidth and RTI noise are calculated by default with the gain of 100V/V, except that the AD8428 gain is fixed at 2000V/V, and the data are referenced from the chip datasheets provided by the manufacturers).

Manufacturer	Part Number	CMRR (dB)	Band width (MHz)	Noise RTI (nV/$\sqrt{Hz}$)	Input resistance	Gain setting
ADI	AD8421A AD8421B	126 min. 134 min.	2	3.05	30 GΩ	1+9.9kΩ/R_G
ADI	AD8429A AD8429B	120 min. 130 min.	1.2	1.10	1.5 GΩ	1+6kΩ/R_G
ADI	AD8428A AD8428B	130 min. 140 min.	3.5	1.3 typ. 1.5 max	1 GΩ	Fixed 2000 V/V
TI	INA103	125 typ. 100 min.	0.8	1.19	60 MΩ	1+6kΩ/R_G Internal R_G
TI	INA163	116 typ. 100 min.	0.8	1.17	60 MΩ	1+6kΩ/R_G
TI	INA217	116 typ. 100 min.	0.8	1.58	60 MΩ	1+10kΩ/R_G
THAT Corporation	THAT1510	100 typ. 85 min.	7	1.7	36 MΩ	1+10kΩ/R_G
THAT Corporation	THAT1512	100 typ. 85 min.	7	1.4	36 MΩ	0.5+5kΩ/R_G

2.4. Conclusion

At the beginning of this chapter, the physical properties of the different progress of lightning formation and development are described. It can be seen that the current range in different stages has changed greatly, from a few microamps during corona discharge, to a few amps when the leader occurs, to tens of kiloamps of lightning return stroke current. However, the current measurement devices cannot cover all the ranges at the same time, and mainly focus on the observation of corona discharge and the development after the formation of the leader, which is detrimental for studying lead generation and its association with subsequent events.

Considering that the present lightning current measurement devices only use passive components at the front end, such as low-resistance-current shunts or Rogowski coils, the addition of amplifiers is beneficial to improve the signal-to-noise ratio of the minimum range. With the mass production of high-bandwidth, low-noise operational amplifier chips, this idea became feasible. In this way, the dynamic range of lightning current measurements can be improved without changing the infrastructure of existing observation sites.

Chapter 3. Framework of Lightning Current Acquisition System

A complete set of lightning current acquisition system mainly includes attenuator, amplifying unit, digital-to-analog conversion (DAC) unit, digital signal processor, optical transmission unit, recording unit, power supply unit and clock unit. **Figure 3-1** shows the system block diagram in general. In order to better meet the needs of field observation, it is very important to consider the limitations of field observation conditions in the early stage of design, and to determine the optimization direction of each unit with this target. In this chapter, the details of the SZMGT observation site will be first introduced. Secondly, the framework of the analog front-end and acquisition system will be introduced, and then the test plan in the laboratory and the construction of the field test will be explained. Finally, the main technical requirements and realization difficulties for the target of this study will be summarized.

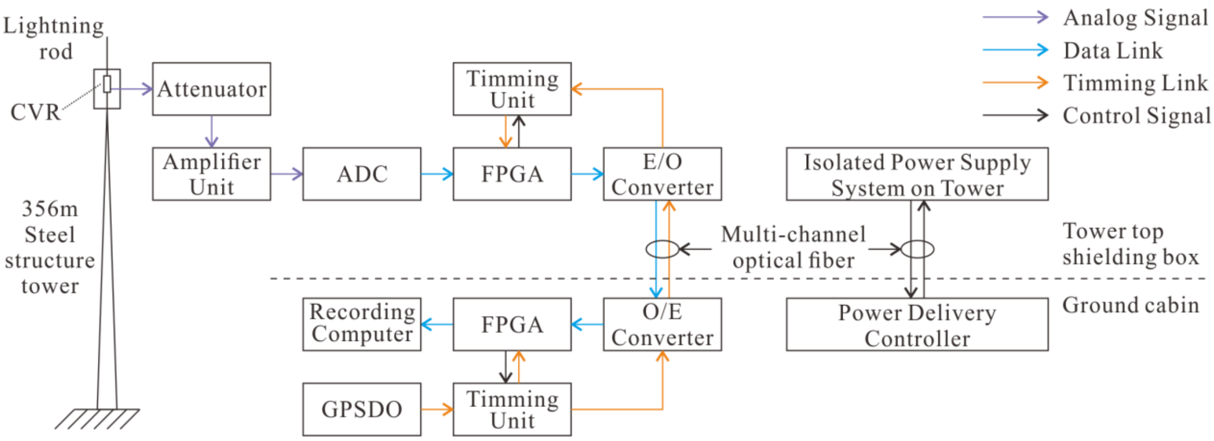

Figure 3-1. Block diagram of the lightning current acquisition system.

3.1. Infrastructure of SZMGT

The Shenzhen Meteorological Gradient Tower (SZMGT) was built in 2016 in the suburban area of Shenzhen, China (**Figure 3-2**), which is located in a lower latitude coastal area at latitude 22.65°N, longitude 113.89°E, and the altitude is 40 m. The height of the tower tip from the ground is 360.8m, which includes the 356 m tower body and a 4.8m high lightning rod (Y. Yang et al., 2018; Z. Qiu et al., 2019). **Figure 3-3** shows the existing lightning current measurement equipment on the SZMGT, which mainly includes a 0.25 mΩ current shunt manufactured by Hilotest with a bandwidth of DC – 50 MHz, a HBM ISOBE5600t analog to optical converter with ± 50 V analog input range and 20 MHz bandwidth installed in a shielding case with 57 cm wide, 29 cm high and 29 cm deep and a set of 12V lead-acid battery pack with 50 Ah capacity containing 60W isolated power charging module on top of the tower. In the cabin next to the tower, there are a HBM ISOBE5600r optical to analog converter, a HBM GEN7tA data acquisition system with GN413 100 MSps high speed differential input sampling card and a GPS disciplined oscillator (GPSDO). A total of 6 multimode OM3 optical cables connect the tower top shielded case to the ground cabin, and each fiber optic cable can provide a one-way 2 Gbps communication bandwidth.

Besides, two atmospheric electric field meters were installed on the tower at positions 20m and 350m high, and another one was installed on the roof of the main observation site at 440 m away from the tower base. And two high-speed cameras V711 and Miro M310 manufactured by Phantom were also installed at the main observation site. However, the measurements of fast electric field, magnetic fields and VHF arrays are heavily polluted by a medium-wave radio tower 200 meters away from the main observation point, and the observation of lightning in this field site mainly focuses on the measurement of current, high-speed camera and slow electric field.

Figure 3-2. Photo of Shenzhen Meteorological Gradient Tower (SZMGT), showing the main steel structure and stray lines of the 356 m high tower. The photo on the upper right corner shows the HBM-based current measurement and data transmission system in a tower-top shielded case.

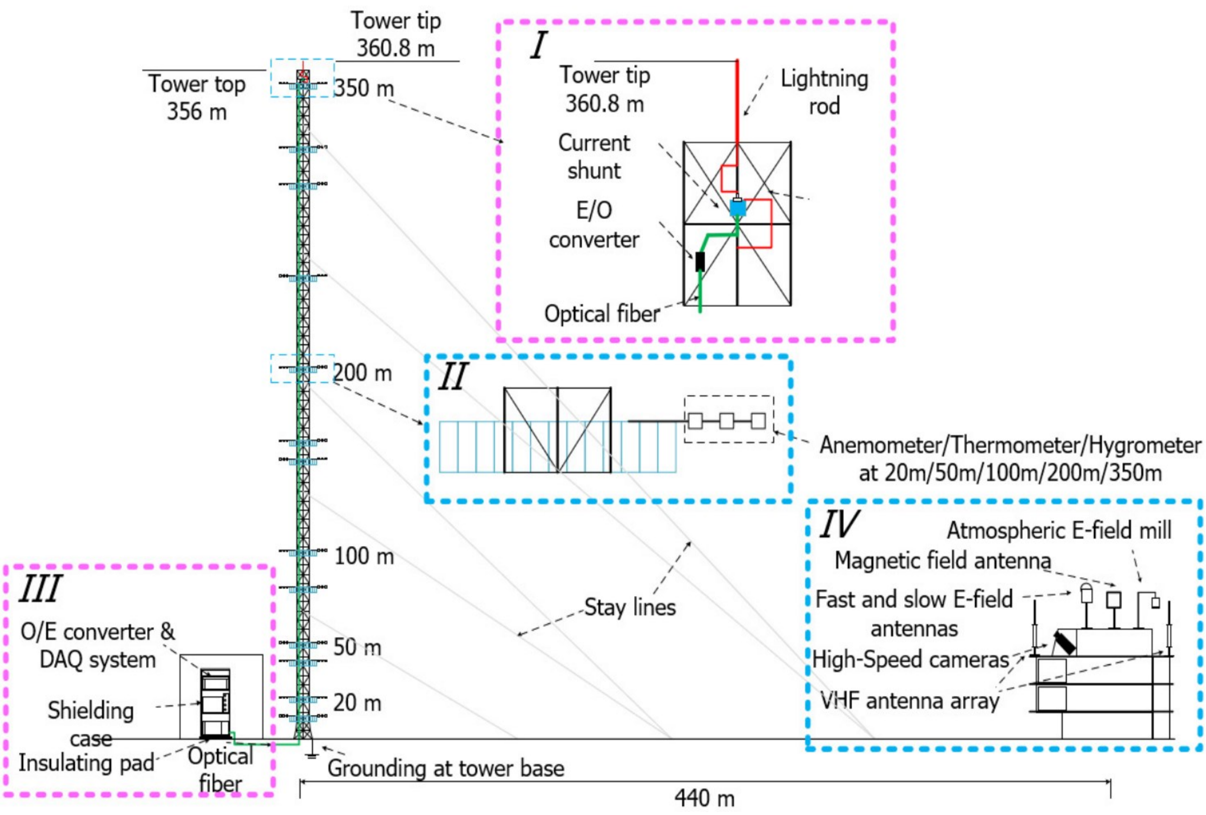

Figure 3-3. Setup of the lightning current and other measurements on and around SZMGT (Z. Qiu et al., 2019).

3.2. Framework of Analog Front-End Design

In order to achieve a wider dynamic range of lightning current measurements, multi-range measurements have been used in several observatories, which have been introduced in Section 2.2.1. In this design, the lightning current will be measured through four channels with different input ranges, and a low-noise amplifier unit will be added in front of each channel. **Figure 3-4** shows the four-channel analog front end designed in this subject, and **Table 3-1** shows the key analog characteristics of the four channels. It can be seen that the higher range has a larger bandwidth, which is the result of the balancing between noise, gain, bandwidth and power consumption. Two types of amplifiers and filters are used for the four channels. For the two channels with smaller ranges, instrumentation amplifiers (INA) are used after the voltage clamp to improve common-mode noise rejection and provide higher voltage gain, and the 3rd order lowpass Multiple FeedBack (MFB) filters are designed to limit the bandwidth and noise before ADC. For the larger ranges, high-speed amplifiers with Junction gate Field-Effect Transistor (JFET) input stage are used after the attenuator. The low base current characteristic of the JFET can reduce the DC voltage offset, and its high bandwidth and low noise characteristic can further improve the system dynamic range. Correspondingly, the 7th order passive elliptic low pass filters are used, which have a steeper attenuation curve in the stopband to make more use of the ADC's first Nyquist bandwidth.

Traditionally, the pre-amplifier unit can be divided into several stages, including input buffers with high input impedance, amplifier with high voltage gain, filters with specific bandwidth and output buffers with low output impedance. Besides, input impedance matching is needed to avoid the standing waves due to impedance changes during transmission, and an ADC driver is usually required in the front of the ADC to convert the single-ended signal into a differential signal to improve the signal-to-noise ratio of the ADC. Typically, 4 to 7 op-amps or drivers each channel are needed before the analog signal is fed into the ADC, which increases system power consumption, raising circuit complexity, and requires larger instrument size. In this design, the functions of different stages are combined by changing the circuit topology, fewer op-amp chips are used to reduces the power consumption and complexity of the system effectively, and the circuit structure and design method will be explained in Chapter 4.

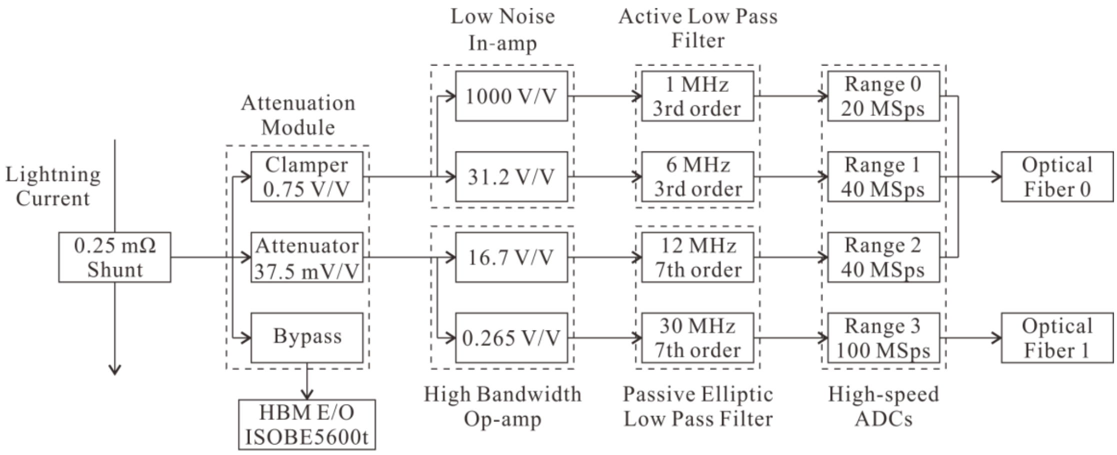

Figure 3-4. Simplified block diagram of analog front end.

Table 3-1. Measurement range and noise estimation corresponding to each range.

Range	Lower limit	Upper limit	Bandwidth	Noise Density	Noise estimation
0	10 mA	5 A	600 kHz	1.504 $nV/\sqrt{Hz}$	5.02 mArms
1	0.15 A	150 A	6 MHz	3.69 $nV/\sqrt{Hz}$	38.9 mArms
2	6 A	6 kA	12 MHz	84.7 $nV/\sqrt{Hz}$	1.243 Arms
3	400 A	400 kA	30 MHz	2591 $nV/\sqrt{Hz}$	60.1 Arms

3.3. Framework of Acquisition System Design

The complete acquisition system includes two subsystems on the tower and on the ground, **Figure 3-5** shows the simplified block diagrams of these two parts. In order to reduce the difficulty of system construction, the same Printed Circuit Board (PCB) with FPGA and optical transceiver is reused in both subsystems, and the FPGA is mainly responsible for the protocol conversion and time stamping in the data link of the whole system. In addition, unlike traditional acquisition equipment that uses hardware to complete signal triggering and buffering, computer software can enable the system to have continuous recording capabilities.

In acquisition systems, precisely marking the time of each sampling point is critical in multi-system observations. For example, in addition to lightning current measurement on the SZMGT, lightning luminescence is also observed by high-speed cameras installed in the main observation site 440m away from the tower, and it is very important to correlate the lightning current with the luminescence phenomenon in lightning research. Although the current GPS-based timing accuracy can reach 20ns, the existing equipment usually does not compensate for the time-consuming of the signal transmission process, which will cause a time error of about 2 μs in the transmission distance of 400m. And when the time delay caused by the internal triggering of the acquisition system is considered, the time error will be larger. In the design of this system, the precise time stamping function is mainly considered. Since the GPS timing system cannot be installed on the top of the tower, the time stamping is first marked on the ADC output data stream first, and then compensates for the transmission time by measuring the transmission loop delay, which improves the time accuracy of the sampling point to about 50ns. And all the design details of the acquisition system will be explained in Chapter 5.

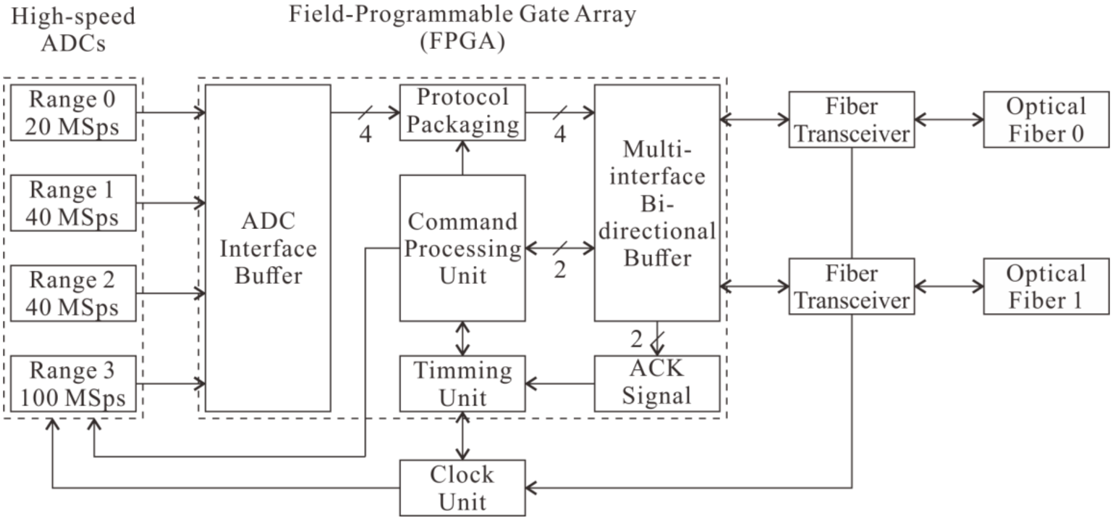

(a) At the top of tower

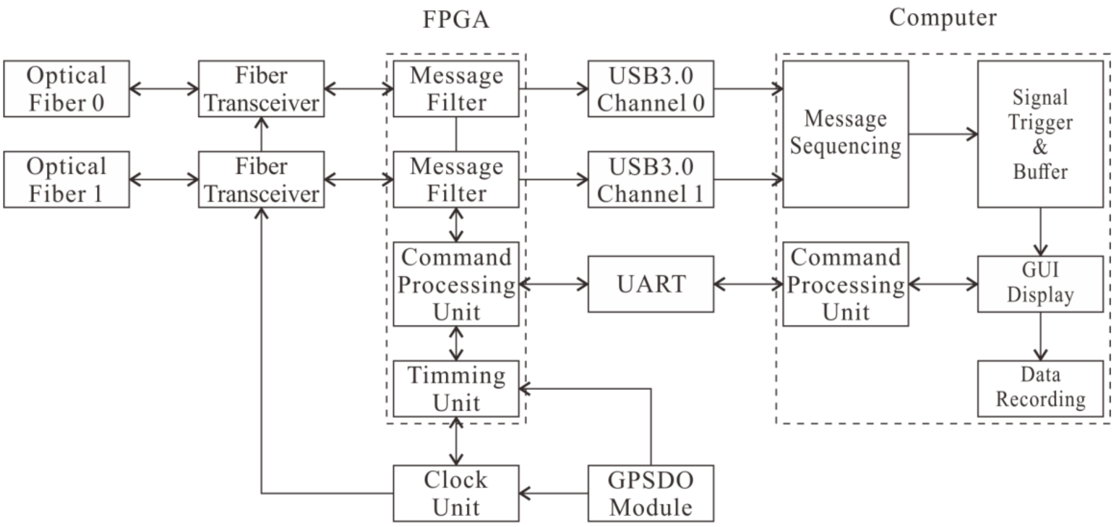

(b) On ground

Figure 3-5. Simplified block diagram of acquisition system.

3.4. Laboratory Test and Field Experiment Programs

Since the installation process of the equipment on the tower is very cumbersome, it is very important to complete the performance and reliability tests in the laboratory in the early stage. And because the entire acquisition system is very complex, including analog, digital and optical signals, the single performance test of the subsystem will be completed first in the Lightning Physics and Protection Laboratory at the Hong Kong Polytechnic University (PolyU), then the system integration test and reliability test will be carried out in the High Voltage Laboratory at Shiyan, Shenzhen near the SZMGT, and the final observation will be done on SZMGT. **Table 3-2** lists all the test items that will be carried out before installation on the tower, and detailed test results will be listed in Chapter 6.

Table 3-2. Laboratory test items and corresponding subsystems.

Subsystem	Test item	Test site
Attenuator	Frequency response	PolyU
Attenuator	High current impulse test	Shiyan, Shenzhen
Analog Front-End	Frequency response	PolyU
Analog Front-End	Voltage noise spectral density	PolyU
Analog Front-End	Impulse response	PolyU
Analog Front-End	Saturation recovery time	PolyU
Timming Unit	Time measurement accuracy	PolyU
Clock Unit	Frequency stability	PolyU
Clock Unit	Phase Locked Loop (PLL) lock time	PolyU
Optical Transceiver	Automatic reconnection	PolyU

Optical Transceiver	Output optical power	PolyU
Optical Transceiver	Bit error rate	PolyU
System debugging	Frequency response of each range	PolyU
System debugging	Noise level of each range	PolyU
System debugging	Power consumption	PolyU
System debugging	High current impulse test	Shiyan, Shenzhen
System debugging	Software stability	PolyU
Field Observation	Lightning current	SZMGT

3.5. Conclusion

In order to observe the lightning leading current on the SZMGT, not only the technical specifications such as noise and dynamic range, but also the infrastructure and installation limitations of the SZMGT should be considered when designing the lightning current measurement and acquisition system. Regarding the infrastructure of the tower, the limitation of device volume, power consumption and the rate of optical fiber transmission are mainly considered. For the volume constraints, a highly integrated analog front-end design will be used. For the limitation of power consumption on the tower, a simplified data processing pipeline will be used on the tower and most of the signal processing will be handled in the cabin on ground. And two optical channels will be used in parallel to solve the limitation of the rate of optical transmission. Before being installed on the tower, the entire system will be repeatedly tested and adjusted in the laboratory to ensure its technical specifications and reliability, and the complete design and testing process will be described in detail in the following chapters.

Chapter 4. Analog Front-End Design

As mentioned earlier, the front-end design of this acquisition system requires trade-offs between noise and bandwidth within limited power consumption and board area. To meet these requirements, a shock tolerant pre-attenuator module and two circuit topologies will be used for the 4 ranges. Usually, the ADC driver will be designed together with the ADC peripheral circuit as a part of the acquisition system, but in this design, the ADC driver will be integrated in the front-end amplifying unit to reduce power consumption and save circuit board space. Therefore, the outputs of all four amplification channels will be differential, and the full-scale voltage is 2 Vpp to meet the ADC input voltage range. Based on the current measurement range proposed in **Table 3-1**, and the 0.25 mΩ shunt installed on the SZMGT, the target of gain and bandwidth of each amplification channel shows in **Table 4-1**, which will serve as the basic specifications of the analog front-end design in this chapter.

Table 4-1. The overall voltage gain and bandwidth target (attenuator included) for each range.

Range Number	Peak Current	Peak input voltage	Peak output voltage	Gain target	Bandwidth
0	5 A	1.25 mV	1 V	800	400 kHz
1	150 A	37.5 mV	1 V	26.67	5 MHz
2	6 kA	1.5 V	1 V	0.667	5 MHz
3	400 kA	100 V	1 V	0.01	20 MHz

4.1. Attenuator Module and Input Protection Design

Due to the high peak value of the lightning current and the large dynamic range, the attenuation module and the input protection unit act as a barrier before the signal enters the preamplifier, not only the safety and reliability of the device, but also the noise increase and the size of the volume should be considered. In high voltage measurements, high value resistors are often used to reduce the peak current generated in the protection state. Due to thermal noise, high resistance values will undoubtedly increase more noise and make the streamer current undetectable. However, low value resistors will generate larger protection currents, which require higher resistance power rates and larger resistor sizes. In addition, due to the strong electric field near the lightning channel, multi-point grounding will cause serious step voltage and lead equipment breakdown. It is very important to perform single-point grounding at the output end of the coaxial shunt. And because the lightning current has high-frequency components, the terminal impedance matching is also very important, which can avoid the reflection of the signal during the transmission process. In summary, the balance of protection current and noise, grounding, and termination matching are considered in this design, and are premised on equipment safety and reliability.

Figure 4-1 and **Figure 4-2** shows a simplified diagram of the attenuation module and input protection circuit. Overall, two types of coaxial cable are used in order to meet the installation requirement on SZMGT. Ideally, the attenuator module should be attached directly to the shunt, but due to the way the shunt is mounted, a short coaxial cable with 50 Ω impedance will be used. And triaxial cables with better shielding properties are used to connect the attenuator to the acquisition device on the tower. In the attenuator module, the input signal from shunt is divided into three paths, the first path with R1 and D1 forms a voltage clamper, the second one with R3 and R4 forms the attenuator, and the bypass port will be used for testing. And each path uses a small value resistor (R2, R5 and R6) as a fuse to enhance system safety. In the protection circuit, two gas discharge tubes (Ga and Gb) are used to avoid hazards due to attenuator module failure. Ra, Rb, Rc and Rd serve as the terminal resistors to match the impedance of the 75 Ω triaxial cable, where Rc and Rd in series also serve as the second attenuator for the range 4. As the second insurance before the amplifier, Ra with Da, Re with Dc and Rf with Dd constitute three sets of voltage clamps to ensure that the voltage entering the amplifier is within the allowable range.

Finally, the overall attenuation ratios are 0.75 V/V for high gain channel and 0.0375 V/V for low gain channel. And the device ground is connected to the case ground through the diode pair Db and De for protection, and the high-value resistor Rg to avoid floating, which not only provides good shielding for the signal by short-circuiting the outer shielding layer, but also avoids the ground loop between the two signal channels through the intermediate layer of the triaxial cables.

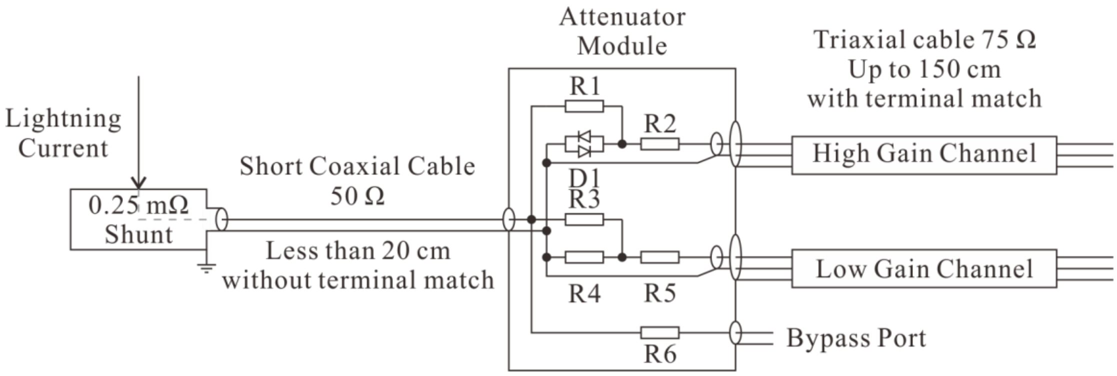

Figure 4-1. The internal structure and connection method of the attenuator module.

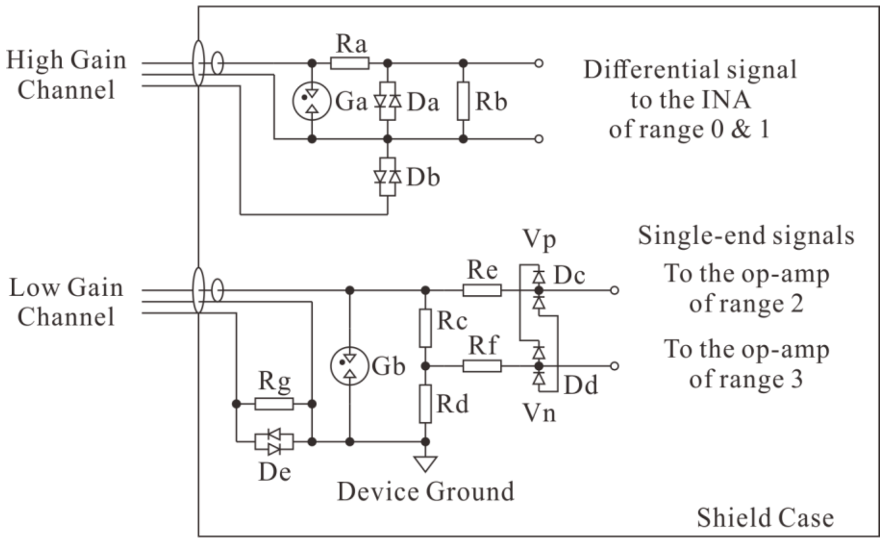

Figure 4-2. The internal structure of protection circuit.

4.2. INA with Active Filter Design for Range 0 and Range 1

Different from the traditional single-ended signal based analog front-end (AFE) design, differential signal chain is used for range 0 and 1. **Figure 4-3** shows the simplified block diagram of AFE designed in this topic, and the main parameters of the circuit are listed in **Table 4-2**. It can be seen that after the protection unit, a passive electromagnetic interference (EMI) filter with another pair of diodes are used to improve the common-mode rejection ratio of the instrumentation amplifier for the radio frequency (RF) band.

In the INA stage, two different circuit structures with different optimization directions will be designed. For range 0, noise performance is considered first, two ultra-low noise single-chip INAs are used in parallel, and a single-end offset compensation circuit is connected to the REF pin of one INA chip. By interconnecting the inputs of the two INAs in reverse, not only the noise can be reduced by a factor of 0.707, but the requirement on the output slew rate of a single INA can also be reduced, which allows the use of lower power supply voltages with little impact on bandwidth, and reduces power consumption at the same time. For range 1, the integrated INA chip cannot meet the higher bandwidth requirements, so a 3-op amp INA configuration will be used. In this configuration, two high speed op-amps are served as the first stage with high input impedance, and the full differential ADC driver will be served as the second stage. The 3rd order fully differential Butterworth low pass Multiple FeedBack (MFB) filter and offset voltage compensation circuit will also be inserted in this stage.

In addition, another 2rd order differential LC filter is inserted between the ADC driver and ADC chip, and the high frequency noise generated in the circuit will be filtered out, which can reduce the impact of noise above the first Nyquist frequency on the ADC's signal-to-noise ratio.

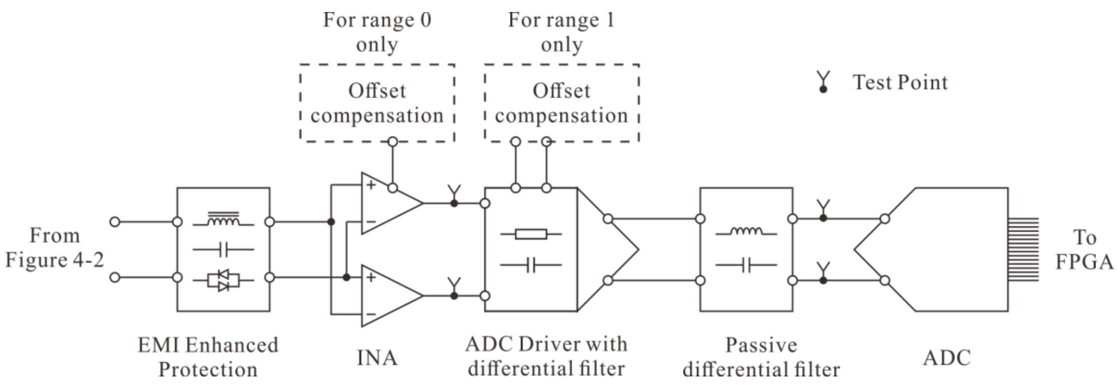

Figure 4-3. Simplified block diagram of analog front-end design for range 0 and range 1.

Table 4-2. Main design parameters and simulation results of the circuit for range 0 and range 1.

Item	Range 0	Range 1
Bandwidth of EMI filter	4.7 MHz	37.9 MHz
Type of EMI filter	2nd order passive filter with ferrite beads and common mode choke	
Gain of INA stage	400.7 V/V	20.08 V/V
Bandwidth of INA stage	647 kHz	9.37 MHz
Gain of ADC Driver stage	2.495 V/V	1.653 V/V
Bandwidth of ADC Driver stage	1.0 MHz	6.5 MHz
Type of ADC Driver filter	3rd order MFB Butterworth active filter	
Bandwidth of LC Filter before ADC	10 MHz	30 MHz
Type of LC Filter before ADC	2nd order Butterworth passive filter	
Reference to AFE input (without Attenuator) offset voltage compensation amplitude	±1.02 mV	±4.95 mV
Overall gain include attenuator	750 V/V	24.90 V/V

Overall bandwidth	~ 600 kHz	~ 6.0 MHz
Overall voltage input range	±1.33 mV	±40.2 mV
Overall equivalent current range	±5.33 A	±160.7 A
Overall noise spectral density	$1.504\ \mathrm{nV}/\sqrt{\mathrm{Hz}}$	$3.69\ \mathrm{nV}/\sqrt{\mathrm{Hz}}$
Overall equivalent current noise	5.02 mArms	38.9 mArms
Overall signal-to-noise ratio	57.5 dB	69.3 dB

4.3. High-speed Amplifier with Passive Filter Design for Range 2 and Range 3

Since the lightning stroke current has more high-frequency components than the leader current, maximizing ADC bandwidth utilization is the main optimization direction for AFE ranges 2 and 3. Because the sampling law indicates that the noise above the first Nyquist frequency will be superimposed in the fundamental frequency range due to undersampling, and the full power bandwidth of the high-speed ADC can usually reach the 10th Nyquist frequency, a high-order filter is required to provide greater attenuation of out-of-band signals. As the filter order increases, the matching of circuit components becomes more difficult, and a small mismatch will cause the filter passband flatness to be deteriorated. Filter with single-ended design can effectively reduce the number of components and simplify the component matching process. Due to the higher frequency, passive filters with better noise performance and acceptable size of components will be used, and the type of elliptic filter will be adopted because it has steeper decay curves than Butterworth filters. Besides, considering that the network analyzer can test high-frequency circuits more conveniently, the filter is also designed with the impedance of 50 Ω.

Figure 4-4 shows the simplified block diagram of AFE design for range 2 and 3, and the main parameters are listed in **Table 4-3**. The design processes of ADC driver and LC filter before ADC have no different from ranges 0 and 1, except that impedance matching at both ends of passive filter is required. Another difference is that the capacitance in the EMI filter is actually made up of the op-amp's input capacitance and the stray capacitance on the board. Due to the higher frequency, the extra capacitors are not needed.

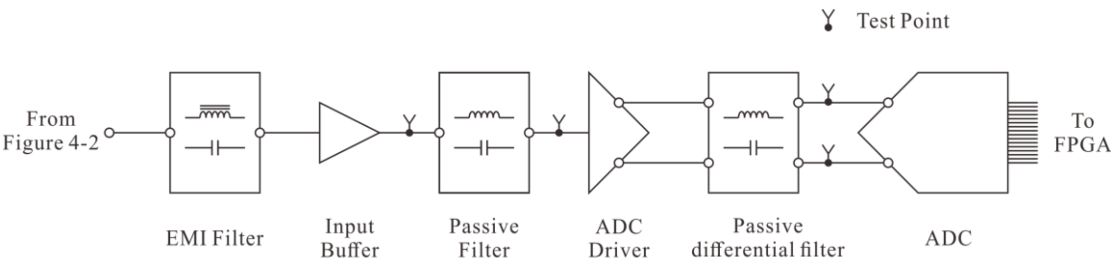

Figure 4-4. Simplified block diagram of analog front-end design for range 2 and range 3.

Table 4-3. Main design parameters and simulation results of the circuit for range 2 and range 3.

Item	Range 2	Range 3
Bandwidth of EMI filter	27.3 MHz	83.5 MHz
Type of EMI filter	2nd order passive filter with ferrite beads	

Gain of INA stage	10.09 V/V	1 V/V
Bandwidth of INA stage	56.35 MHz	1.49 GHz
Bandwidth of passive filter	12 MHz	30 MHz
Type of passive filter	7th order Elliptic passive filter	
Gain of ADC Driver stage	1.660 V/V	0.795 V/V
Bandwidth of LC Filter before ADC	30 MHz	75 MHz
Type of LC Filter before ADC	2nd order Butterworth passive filter	
Overall gain include attenuator	0.628 V/V	0.00994 V/V
Overall bandwidth	~ 12 MHz	~ 30 MHz
Overall voltage input range	±1.592 V	±100.6 V
Overall equivalent current range	±6.37 kA	±402.5 kA
Overall noise spectral density	84.7 $nV/\sqrt{Hz}$	2591 $nV/\sqrt{Hz}$
Overall equivalent current noise	1.243 Arms	60.1 Arms
Overall signal-to-noise ratio	71.2 dB	73.5 dB

4.4. Conclusion

In this analog front-end design, the multi-range simultaneous acquisition method is used to expand the dynamic range of lightning current measurement. Different optimization directions are used for different ranges to meet the requirements of various lightning process currents. For example, the detection of lightning streamer current requires high sensitivity and a very low noise floor, while the measurement of lightning stroke current requires a large range and high bandwidth. In addition, due to the harsh electromagnetic environments near the lightning channel, it is necessary to focus on grounding and protection issues on the premise of meeting the performance requirements.

In this chapter, protection methods of AFE design is introduced first, and the grounding method is described later. Basically, the grounding principle is to avoid ground loops, and the protection measure is to limit the voltage amplitude by clamping. For example, each high-sensitivity channel (range 0 and 1) has a total of three protections, which are the attenuation module, the protection circuit and the EMI enhanced protection in the amplifier unit. For the high-range channel (range 2 and 3), due to the larger protection resistance value and smaller protection current, it is sufficient to set a clamping diode in the protection unit. In addition, input voltage offset compensation is used for high sensitivity ranges to avoid zero drift due to op-amp offset voltage and temperature drift, and the details will be described in Chapter 5 together with peripherals such as isolated power supplies. After that, the design parameters and optimization highlights of the four ranges are presented in detail, and the summary information has been presented in Section 3.2.

Chapter 5. Acquisition System Design

In order to match the installation method of the lightning current acquisition system on SZMGT, the whole system is divided into two parts, which are the power-optimized front-end analog-to-optical converter installed at the top of tower, and the optical receiver and recording computer installed in the cabin on ground. These two parts communicate through two pairs of optical fibers to achieve 4 Gb/s bandwidth, which is the bandwidth required for 4-channel ADCs operating at 20 MSps, 40 MSps, 40 MSps, and 100 MSps, respectively. And in addition to the computer for triggering and data storage, the optical transceivers on the tower and ground are controlled by FPGA, which has the real-time performance required for data timestamp marking. The overall architecture of the lightning current acquisition system has been presented in Chapter 3. This chapter will detail the internal implementation of the FPGA with peripheral hardware and computer software, as well as optical communication and timing protocols.

5.1. Optical Converter Installed on Tower

5.1.1. Hardware Design

Unlike lightning current measurement devices installed close to the ground, tower-mounted current measurement devices have higher requirements for volume, power consumption, and system grounding. In order to meet these requirements, a four-channel data acquisition system is designed, where **Figure 5-1** shows the architecture of this device. Overall, this tower-mounted lightning current measurement device is mainly composed of a 4-channel analog front-end (AFE), four single-channel analog-to-digital converters (ADC), a processer (FPGA), two optical transceivers, and a phase-locked loop (PLL) module. The main purpose of using four independent ADC chips is to reduce the impact on the measurement accuracy of the high-range channel when the low-range is severely saturated, and the use of two optical transceivers with 2.125Gbps bitrate is due to the limitation of the bandwidth of a single multimode optical fiber. An additional low-speed optical transceiver is used to check the fiber optic lines during installation and to debug the FGPA's underlying logic. LEDs of different colors are used to indicate the device operating status, and the IO expander and configuration memory exist as the basic peripherals of the FPGA.

Due to the lack of conditions for installing GPS antennas and network timing synchronization on the tower, the exact sampling frequency and synchronized second pulse need to be transmitted from the timing system installed on the ground. In this acquisition system, the reference clock with frequency of 106.25MHz can be transmitted along with the serialized bit stream by using 8b/10b encoding techniques, and the second signal will be transmitted using reserved symbols in the encoding map, which can be distinguished from the data and commands. However, the instabilities in optical transceivers and transmissions will cause several picoseconds of jitter in the reference clock, which is acceptable for digital systems, but will result in a degradation of the signal-to-noise ratio when this noisy clock is used for signal sampling. In this case, a PLL unit with jitter attenuators is used to generate low-jitter sampling clocks and optical transmit clocks, and the details of the synchronous timing route are explained in Section 5.4.2.

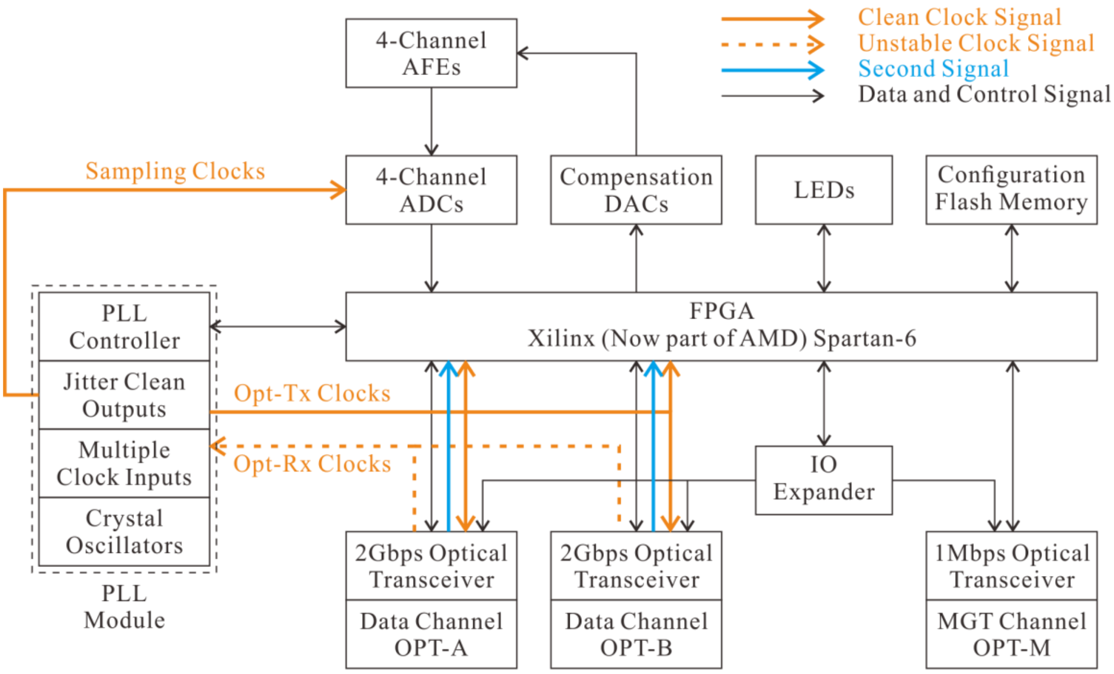

Figure 5-1. Block diagram and signal path of optical converter installed on tower.

In the case of using the existing 12V lead-acid battery pack on the SZMGT for power supply, this optical converter uses both DC/DC switching regulators and low-dropout (LDO) linear regulators to avoid interference to the analog circuit and improve the power conversion efficiency. In addition, isolated power modules are used to reduce the difficulty of grounding the system on the tower, where the **Figure 5-2** shows the complete power path of the tower-mounted optical converter.

For analog front-ends, voltage references and analog-to-digital converters, after using isolated switching power modules to step down and invert the input voltage, LDO with high power supply rejection ratio is used for secondary voltage regulation. And with common mode inductors and magnetic beads, the power supply ripple can be effectively reduced to meet the power supply noise requirements of low-noise preamplifier circuits. Besides, the PLL circuit is also sensitive to power supply ripple. The high frequency ripple on power line will increase jitter on the PLL output clocks. To avoid signal-to-noise degradation due to sampling clock jitter, ferrite beads are also used in all PLL power branches. Finally, the digital devices including FPGA and optical transceivers have a strong tolerance for power supply noise, and it is acceptable to use the switching power supply directly.

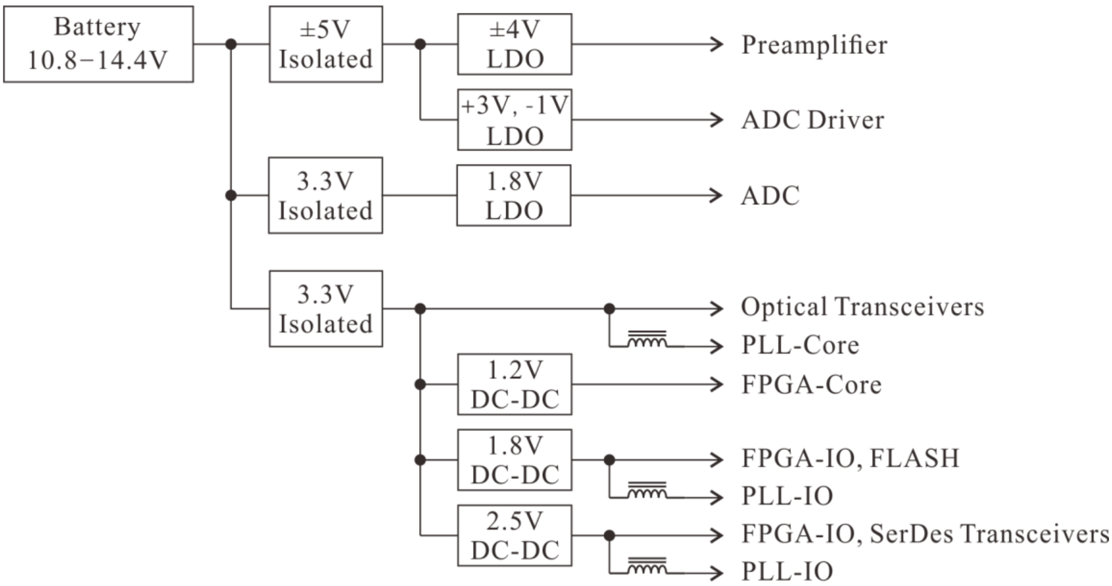

Figure 5-2. Power path of optical converter installed on tower.

5.1.2. Software Design inside FPGA

Thanks to the powerful parallel processing advantage of FPGA, the time information can be marked when the analog signals are sampled in this design, rather than recorded on the computer after transmission. **Figure 5-3** shows the simplified software block diagram inside the FPGA installed in optical converter, only one channel optical transceiver is drawn for simplicity, and another independent protocol packer, checksum calculation unit and output buffer are used for the other optical transceiver.

In this FPGA design, components can be mainly divided into ADC input buffer and synchronization unit, protocol packet output unit, timing unit and other peripherals. Each component runs in parallel, and all components are controlled by a simplified processing state machine. In addition to controlling the start and stop of each unit, this processor also collects the operating status of each unit, and uses the message buffer to transmit it to the protocol packetizer, and finally transmits the system status to the ground. And in the process of data streaming transmission, by using the ring buffer and queuing algorithm, it is beneficial to reduce the waste of time and memory resources caused by data replication. During the sampling process, the data output by ADCs with different sampling frequencies will be stored in their respective ring buffers of each channel after edge-aligned, and the timestamp information of the first data in buffer will be stored together at the same time. The size of a single buffer is designed to be able to be sent in one packet. When a buffer is full, the buffer will be put into the transmit queue, packaged by the protocol packetizer, and transmitted to the optical transceiver.

In the whole process, the data is only cached once, which not only saves resources on the FPGA chip, but also can use a low density FGPA to reduce system power consumption.

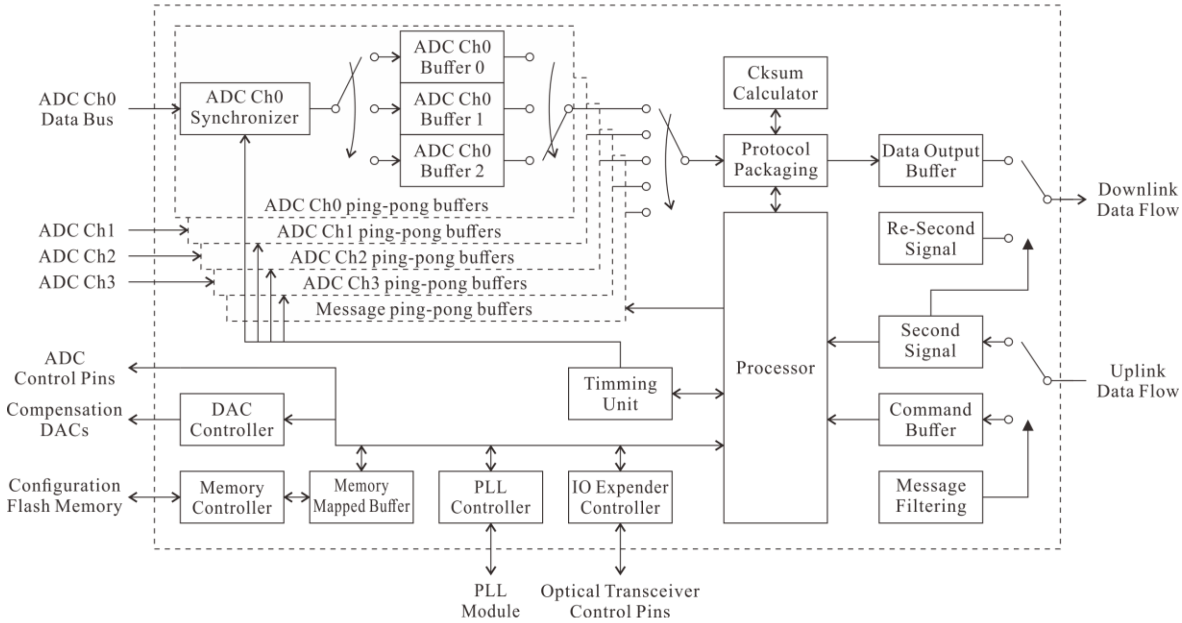

Figure 5-3. Block diagram of software design inside the FPGA installed in optical converter.

As mentioned earlier, each unit in FPGA is running in parallel, and **Figure 5-4** shows the workflow of the processor state machine. After the system is powered on, the underlying logic of the FPGA will first be configured and initialized through the external memory. Then, the processor will load the configuration information in the high address of the FLASH memory into the memory mapped buffer through the memory controller. The configuration data of the PLL will be extracted and the PLL initialization will be completed first, and then wait for the establishment of the optical communication link. The reference clock in the bitstream sent from the ground over the optical fiber will be extracted and used for PLL input clock. After the PLL locked, the second pulse will be synchronized to the sampling clock, and data acquisition process will begin.

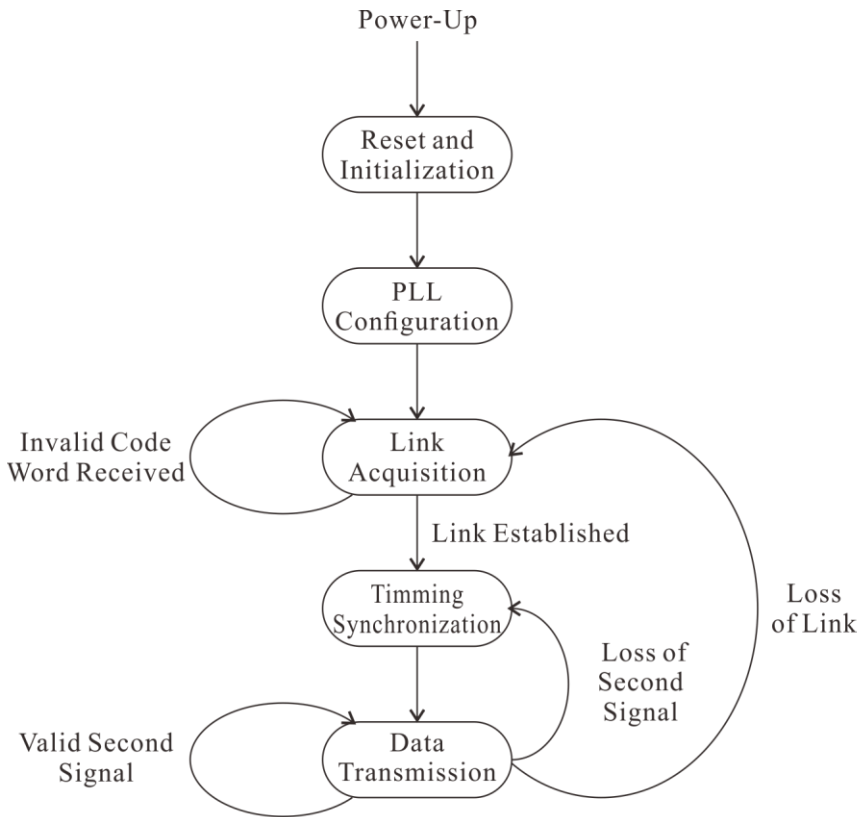

Figure 5-4. Timing state diagram of processor inside FPGA installed in optical converter.

Considering the harsh environment on tower, the ability of automatically recover from failures is necessary. In this acquisition system, both second signal loss and link loss can be recovered autonomously. And during a failure, if only the seconds signal is interrupted, the timer located inside the FPGA will generate the seconds signal to mark the data timestamp. Since there are two pairs of optical communication links, when one of the uplinks fails, the second signal and reference clock can be transmitted over the other fiber. And when one of the downlinks fails, the three low-range signals will be preferentially transmitted. This not only ensures the reliable operation of the system, but also collects most of the lightning current data during the fault period.

5.2. Optical Receiver Installed on Ground

5.2.1. Hardware Design

Similar to the system design on the tower, the optical receiver installed on the ground also uses FPGA as the core controller. The peripheral circuit mainly includes two data-link optical transceivers, one low-speed optical transceiver for testing, PLL module and GPS timing module. And the connection with the computer is carried out through the two-channel USB3.0 interface and a serial interface. **Figure 5-5** shows the simplified system block diagram on ground. Compared with the PCIe interface, which is more difficult to write the FPGA and computer driver, the USB3.0 interface protocol chip has more choices, and the computer driver software is more mature. And in order to improve the data transmission bandwidth and simplify the design of the interface driver, the two USB3.0 channels are only responsible for transmitting the measurement data to the computer, while the commands and status information are transmitted bidirectionally through the serial port. In this way, the software on the computer can use different threads to control different ports, and complete the command sending while receiving the measurement data, which makes the multi-core optimization of the computer software easier to achieve.

In terms of reference clock transmission, the second signal is first obtained by the GPS module, and is captured and locked by the GPS disciplined oscillator (GPSDO) module, then the stabled second signal and 10MHz clock are output as the system frequency reference. After the 10MHz reference clock is generated, the PLL module converts it into the 106.25MHz required by the transceiver, which will be contained in the serialized bit stream and sent out through the optical fiber. And the complete timing route designed in this acquisition system can be find in Section 5.4.2.

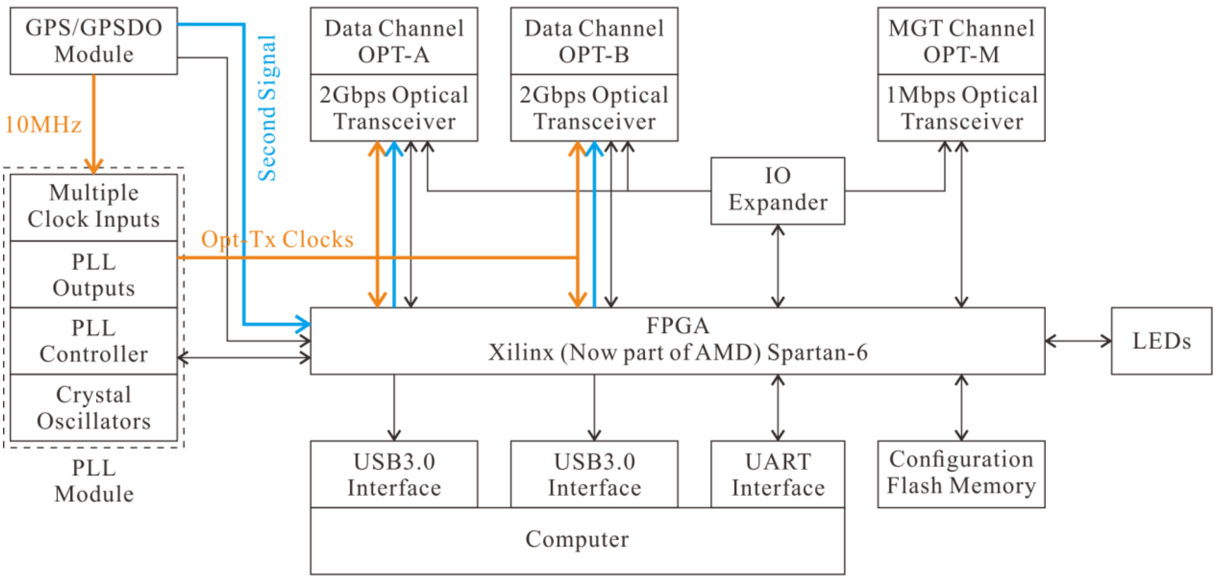

Figure 5-5. Block diagram and signal path of optical receiver installed on ground.

Unlike the harsh working environment on the tower, the power consumption and grounding requirements in the ground cabin are much more relaxed. The optical receiver uses an adapter with 5V output as the power supply, and **Figure 5-6** shows the system power path. Since the GPS/GPSDO module and the main board are implemented on two independent circuit boards, the power input is split into two branches. For GPS and GPSDO module with low power consumption, LDO regulators and magnetic beads are used to simplify circuit design and reduce power supply noise interference to the module. For the main board with the low voltage FPGA, DC/DC switching power supplies are used to improve power conversion efficiency. Similar to the system on the tower, magnetic beads are used in all circuits related to the PLL to suppress interference caused by power ripple. And the use of magnetic beads in the USB3.0 interface circuit is to avoid power fluctuations generated by the transceiver from affecting other parts of the circuit.

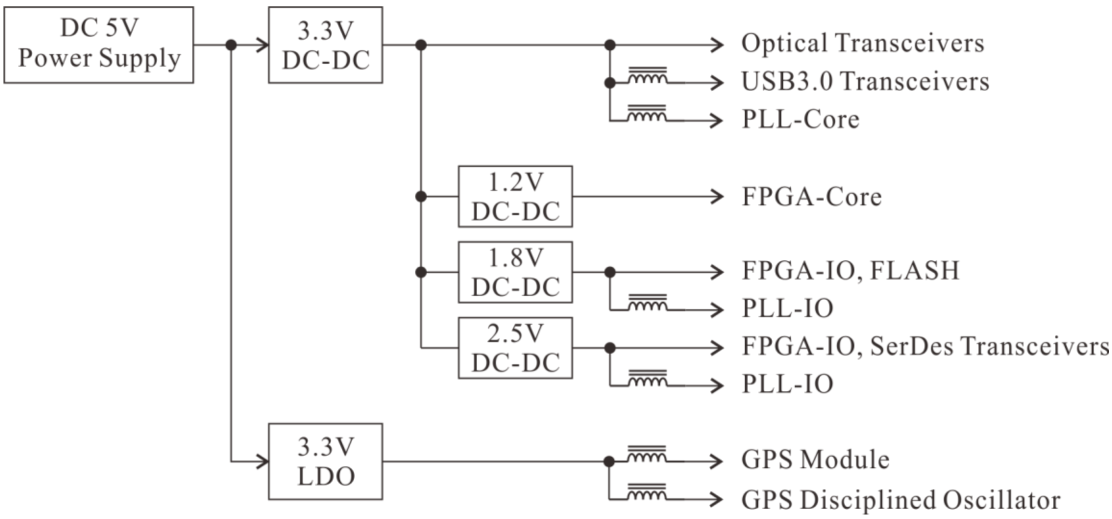

Figure 5-6. Power path of optical receiver installed on ground.

5.2.2. Software Design in FPGA

By using an independent USB 3.0 bridge chip, the data interface between the FPGA and computer is simplified into a FIFO interface, which makes the programming of the FPGA and computer software easier. And the whole system uses computer software for signal triggering and data processing, which greatly reduces the programming difficulty of the FPGA in the optical receiver. **Figure 5-7** shows the software framework in the FPGA, and the second downlink data flow and USB3.0 interface are simplified.

The downlink data stream from the tower is first differentiated from the feedback second signal by a message filter, and then the checksum is checked while the data is being fed into the buffer. Since the transmission error of individual measurement data point is better than the loss of the entire packet, the data packets that failed validation will also be retained and sent to the computer together with the failure flag. Since optical communication uses digital signals with strong anti-interference ability and low bit error rate, the verification failure is usually caused by the error of several bits, which has little impact on the entire data segment. And the failure flag can also be used as indicator during data analysis to judge the credibility of the data.

Similar to data processing in the FPGA on the tower, a single stage ring buffer is used to optimize data replication. And due to the one-to-one correspondence between the optical communication channel and the USB3.0 channel, the transmit queue is no longer needed. A high-precision timer is used to measure the round-trip time of the second pulse in the fiber, which will be used to correct the timing system on the tower. Otherwise, the peripheral components including PLL controller, memory controller, etc. have no difference from the FPGA system on the tower.

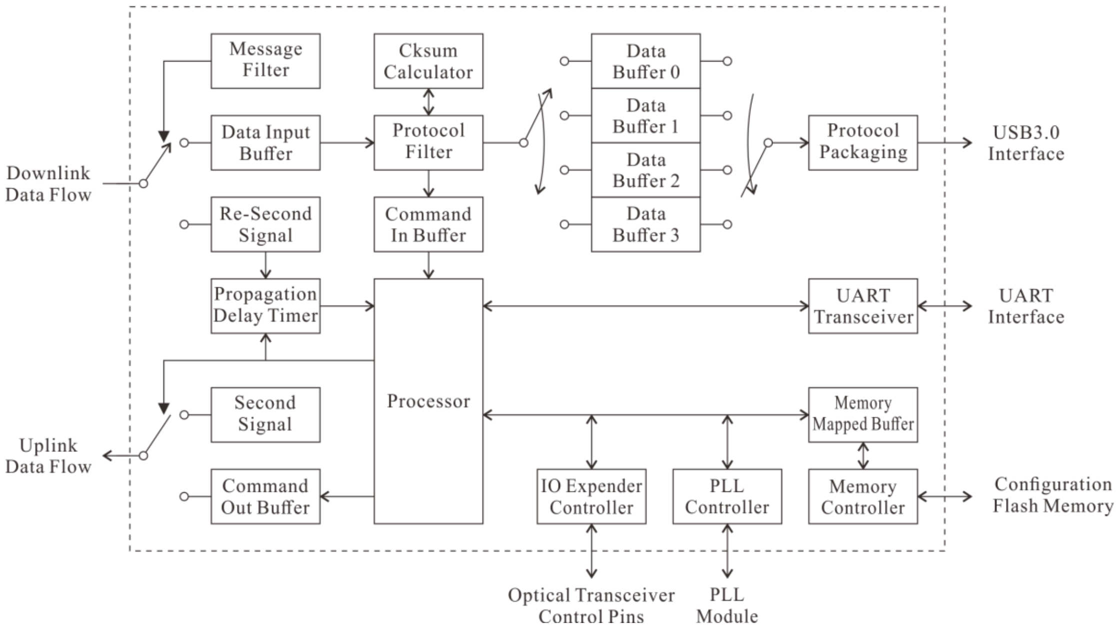

Figure 5-7. Block diagram of software design inside the FPGA installed in optical receiver.

The timing state diagram of the ground system is shown in **Figure 5-8**. Different from the timing system on the tower, the reference clock of the ground timing system is obtained from GPSDO, which has a good frequency holdover ability by using an oven-controlled crystal oscillator. Even when the GPS is interfered and the second signal output is suspended, it can still output an accurate clock frequency for several hours. Therefore, except for the free-run phase after the system is powered on, accurate timing information can be sent to the tower system almost at all time. Considering that GPS interference for a long time hardly occurs, the ground timing system keeps sending time information after GPSDO and PLL locked for the first time, and the state machine switches between locked mode and holdover mode depending on the validity of GPS second signal.

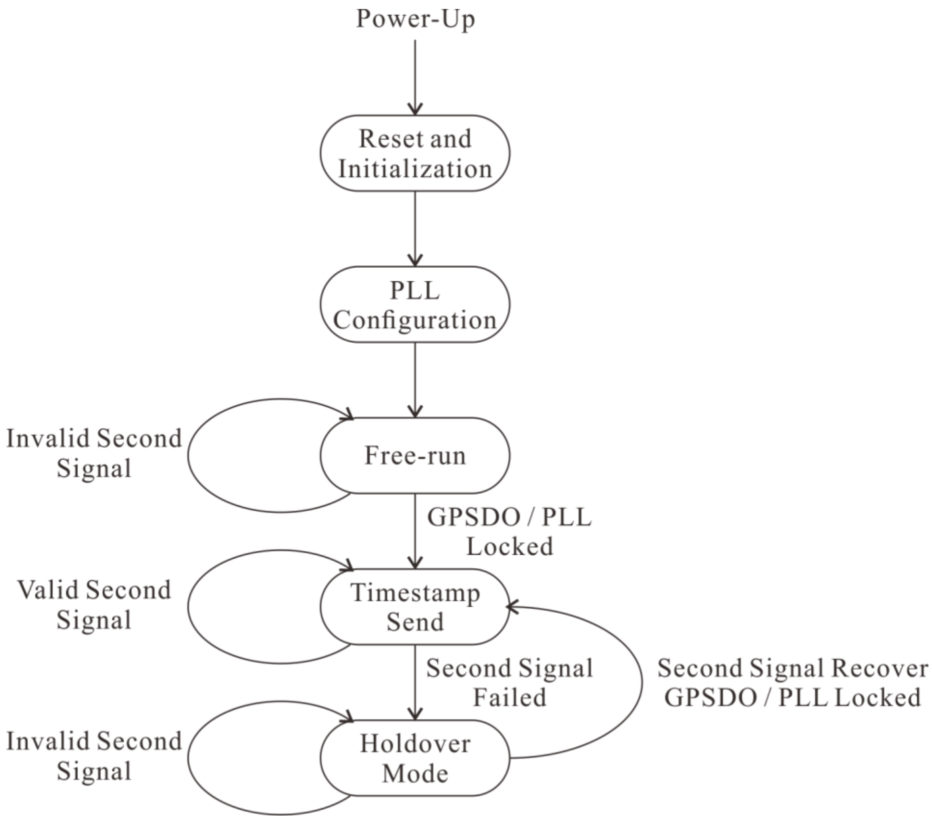

Figure 5-8. Timing state diagram of processor inside FPGA installed in optical receiver.

5.3. Implementation of Computer Software

Different from the traditional acquisition system that uses on-chip cache memory to store the data before and after the trigger event and then transmit and save it, this lightning current acquisition system uses the software running on computer to process and trigger the sampling data stream in real time. Such system architectures are common in low-speed acquisition systems, which is more flexible and has the ability to record continuously of almost unlimited length. But when the data bandwidth reaches 400MBps, the real-time software design becomes difficult and multi-threaded optimization is important.

Figure 5-9 shows the computer software block diagram, which can be mainly divided into six parts: the data stream interface with USB3.0 ports, the command interface with serial ports, data processing unit, command and system status collection unit, data saving unit, and the graphical user interface (GUI) unit. Each interface including USB3.0 and serial ports correspond to a thread, and each other unit corresponds to a thread, which makes this software system a total of 9 threads. At the same time, the data processing thread as the core of the software will use the Intel Math Kernel Library (MKL) to perform multi-core optimization on the calculation process. This allows the entire software to run in parallel with multiple cores, which is in line with the development direction of multi-core processing in today's computer CPUs.

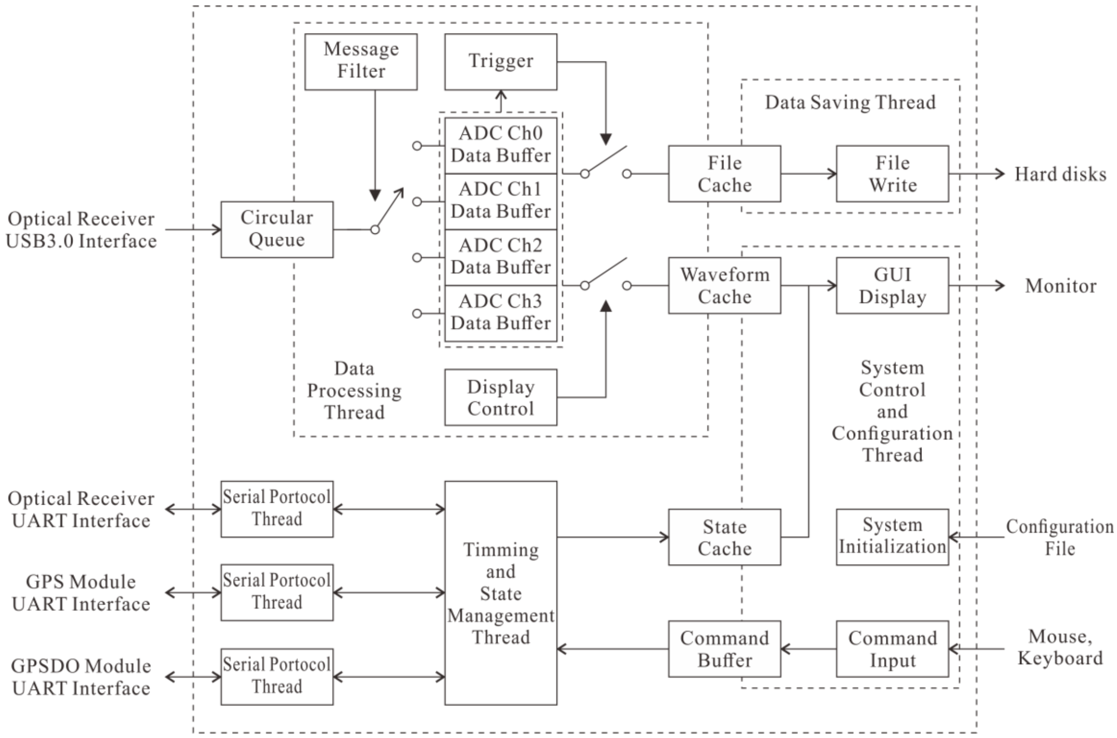

Figure 5-9. Block diagram of computer software design.

In addition to the multi-core optimization, the zero-copy technology is also used in this design. Zero-copy technology means that when a computer performs an operation, the CPU does not need to first copy the data from one place of memory to another specific area. This technique is often used to save CPU cycles and memory bandwidth when transferring files over a network. In this design, the buffer of unit size will be established in the data processing thread, and the address pointer of the buffer will be transferred to the USB3.0 interface thread through a circular queue. Once the measurement data is written into a buffer block, until it is written to the hard disk or released, it will be delivered in different threads with the form of an address pointer to avoid repeated copying of data in multiple buffers, which reduces the consumption of CPU resources and memory bandwidth effectively. And when the data in the buffer block is not needed, the buffer block address will be put into the circular queue again for the interface thread to use, which also reduces the frequent operations of memory reallocation, and further reducing the CPU usage caused by system memory management.

5.4. Communication and Timing Protocols

5.4.1. Communication Protocols

In this design, the new protocol is prototyped with Ethernet frame and Fiber Channel protocol, and is used after adjusting the packet size and header definition to better meet the multi-channel data transmission. The data link transmits at 106.25MHz using Single Data Rate (SDR) mode 16-bit width and achieves a serialized bitstream rate of 2.125Gbps in the optical link, which also determines that the system uses 2-byte aligned. The frame structure of a data packet is shown in **Figure 5-10**, which is mainly composed of frame start sequence, frame header, payload, and CRC checksum. And the entire frame length is controlled within 4096 bytes to match the common buffer block size in FPGA and computer.

Start of Frame	Frame Header	Frame Payload	CRC Error Check	Frame Gap
8 Bytes	16 Bytes	⩽4076 Bytes	4 Bytes	Equivalent 12 Bytes

Figure 5-10. Communication data packet and frame structure.

	Bit 7:0	Bit 15:8	Bit 23:16	Bit 31:24
Word 0	DMAC (Destination MAC)			
Word 1	SMAC (Source MAC)			
Word 2	FrTy (Frame Type)	FrVer (Frame Version)	FrLen (Frame Total Length)	
Word 3	FID (Frame Identification)		FHCK (Frame Header Checksum)	

Figure 5-11. The frame header structure of data packet.

Similar to the preamble in Ethernet frame, the frame start sequence contains 8 bytes, which are 7 0x55 and one 0xD5 in hexadecimal. The frame header structure is shown in **Figure 5-11**, where the DMAC defaults to hexadecimal 0xFFFFFFFF, SMAC is padded with the device serial number. FrTy and FrVer are the abbreviation of frame type and version for distinguishing between data, timing information and commands.

FrLen is the abbreviation of frame total length, which contains the length of frame header and payload. FID is the frame identification number and increments continuously. And FHCK is the checksum of frame header, which is calculated using the same method as the IPv4 header checksum.

After the frame header, payload is the carrier of information, which can be downlink measurement data, uplink commands or bidirectional timing information. The length of payload is limited in 4076 bytes, which is sufficient for timing and command messages. But for measurement data, it is necessary to use FID to assist in verifying the continuity of the data stream. After the packet is received, the CRC checksum is used to verify the integrity of the data. As mentioned earlier, although the data that fails the verification will also be retained, it is very important to ensure the credibility of most of the data in a complete acquisition system. And due to the possibility of loss of the optical communication link, the frame gap exists so that the transceivers have sufficient time to detect and reconnect, while also avoids DC imbalance in serialized bitstream for a long time.

5.4.2. Synchronized Timing Route

Due to the lack of timing equipment on the tower, the seconds signal and reference clock have to be transmitted over fiber optic links, and the main delivery path is shown in **Figure 5-12**. The whole acquisition system uses GPS module to obtain the second pulse synchronized with the satellite, but this second pulse is unstable due to the jitter of the GPS signal passing through the ionosphere. And the GPSDO can filter out fluctuations on the raw pulse-per-second (PPS) signal by tracking for a long time. After GPSDO is locked, a stable second signal and a 10MHz reference clock are output and used as the time reference of whole acquisition system.

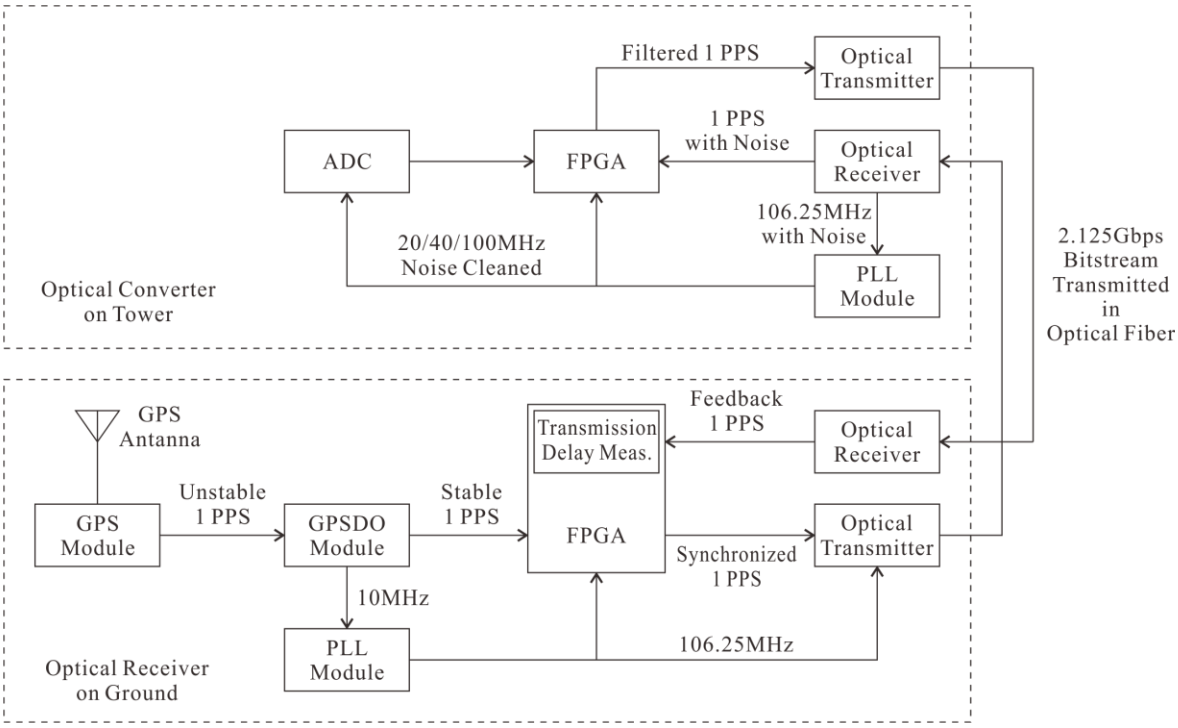

Figure 5-12. Block diagram of timing route.

The 10MHz reference frequency will be input to the PLL block and generate the 106.25MHz required by the fiber optic transceiver, which will be contained in serialized bitstream and sent to the optical converter system on tower. Similar to the GPS signal passing through the ionosphere, the reference frequency will also be jittered during the conversion by the optical transceiver and transmission through the fiber. Since a jittered sampling clock will degrade the ADC's signal-to-noise ratio, a PLL block that includes a jitter attenuator is required. This PLL module first removes the jitter superimposed on the reference clock, and then converts the frequency to 20MHz, 40MHz and 100MHz as the sampling clock of the ADCs.

As mentioned before, the previous equipment used GPS synchronization system to time stamp the signals that have been transmitted to the ground, which is acceptable when the tower is low. However, for the SZMGT with a height of 356 meters, 1.78μs is needed for signal transmission from the tower tip to ground. In this system, a feedback second pulse signal is sent immediately from the system on tower after the receiving the second signal sent by ground. At the same time, a high-precision timer is designed in the FPGA of the ground system to measure the round-trip time of the second signal, which will be sent to the tower system and correct the delay error caused by the second signal transmission.

5.5. Conclusion

In this lightning current acquisition system design, FPGA as the processing core of the measurement system, the timestamp accurate to the sampling point is implemented, which benefits from the parallel architecture. In addition, this system also optimizes the transmission of the reference clock and the second signal, and corrects the delay of the second signal in the transmission process by measuring the time of the second signal in the communication loop. In the data link, ping-pong buffers and ring queues are widely used in FPGA and computer software to avoid data duplication while reducing the FPGA chip density and computer performance requirements. And in computer software design, multi-core parallel optimization and zero-copy technology are used to enhance the real-time processing capability of computer software for measurement data.

In this chapter, the tower system, ground system and computer system are introduced in turn. For the system on the tower and on the ground, the hardware architecture, power supply path, FPGA internal logic and system state machine are introduced comprehensively, which shows the design details of the acquisition hardware. After that, the computer software architecture, communication protocol and complete timing process are introduced, which shows the design details and optimization focus of the system software. Finally, the harsh environment-tolerant hardware and efficient software make up the whole acquisition system.

Chapter 6. System Integration and Tests

The architecture of each part of the lightning current acquisition system designed in this project has been detailed introduced in the previous chapters. In this chapter, the hardware entities and software implementations will be presented, and the completed laboratory test results will be analyzed and compared with the design goals to verify the feasibility of the design and the correctness of the specific implementation. Since the computer software programming has not been completed, this chapter focuses more on hardware implementation and testing, and the unfinished parts and plans are listed in Chapter 7.

6.1. Hardware Assembly

Figure 6-1 shows the implementation of the attenuator, where the housing is CNC machined in brass and nickel plated for good corrosion resistance. And the “Dead Bug” method is used in component soldering to reduce the influence of stray parameters on high frequency signals. In addition, the high-power protection resistor is in direct contact with the metal casing, which is conducive to rapid heat dissipation and is very important to resist multiple return strokes during a lightning process.

Figure 6-2 and **Figure 6-3** show the implementation of the optical converter that will be installed on tower. In the circuit board design, the FPGA digital signal processing unit, the PLL unit and the optical fiber transceivers are designed as a single printed circuit board (PCB), which can be reused in the two systems on the tower and on the ground to reduce the workload. The PCB on the left in **Figure 6-2** integrates the analog front-ends and analog-to-digital converters, which connects to the logic board through a 160-pin board-to-board connector.

Figure 6-1. The internal structure and appearance of attenuator.

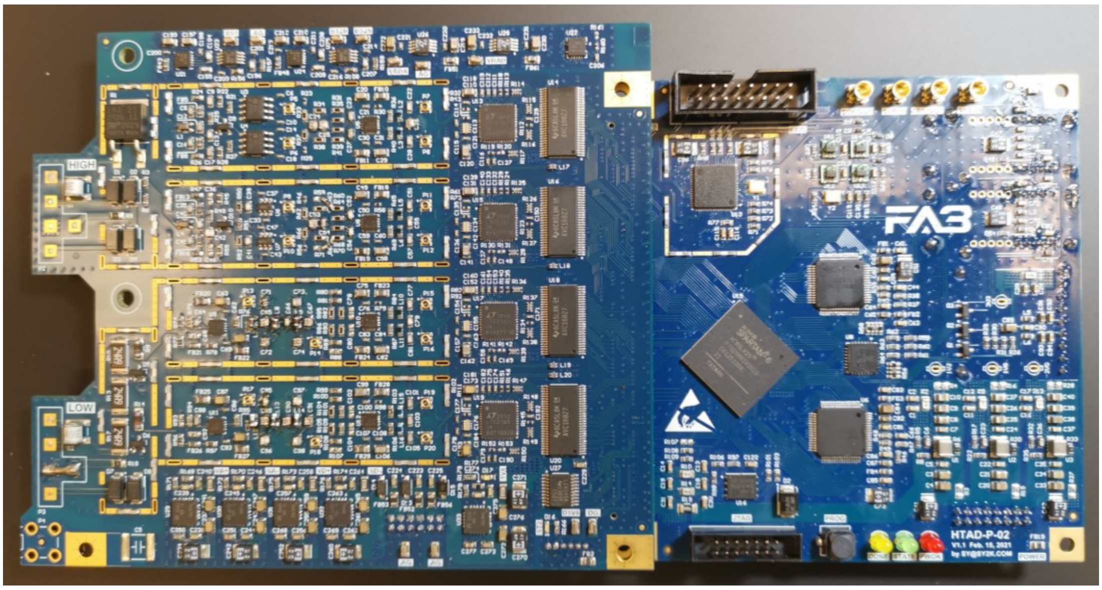

Figure 6-2. The main board of optical converter on tower.

Figure 6-3. The front panel of optical converter on tower.

Figure 6-4 and **Figure 6-5** show the implementation of the optical receiver that will be installed on ground. In addition to the same logic board in the system on the tower, the USB 3.0 interface board connects to the logic board using the same board-to-board connector, which provides the data link and command interface. In addition, the GPSDO module, GPS module and a multi-serial port module are installed at the lower part of **Figure 6-4** in order from left to right. The multi-serial port module can transmit three serial port channels through a single USB port, and the serial ports are connected to GPS, GPSDO and system command interface respectively.

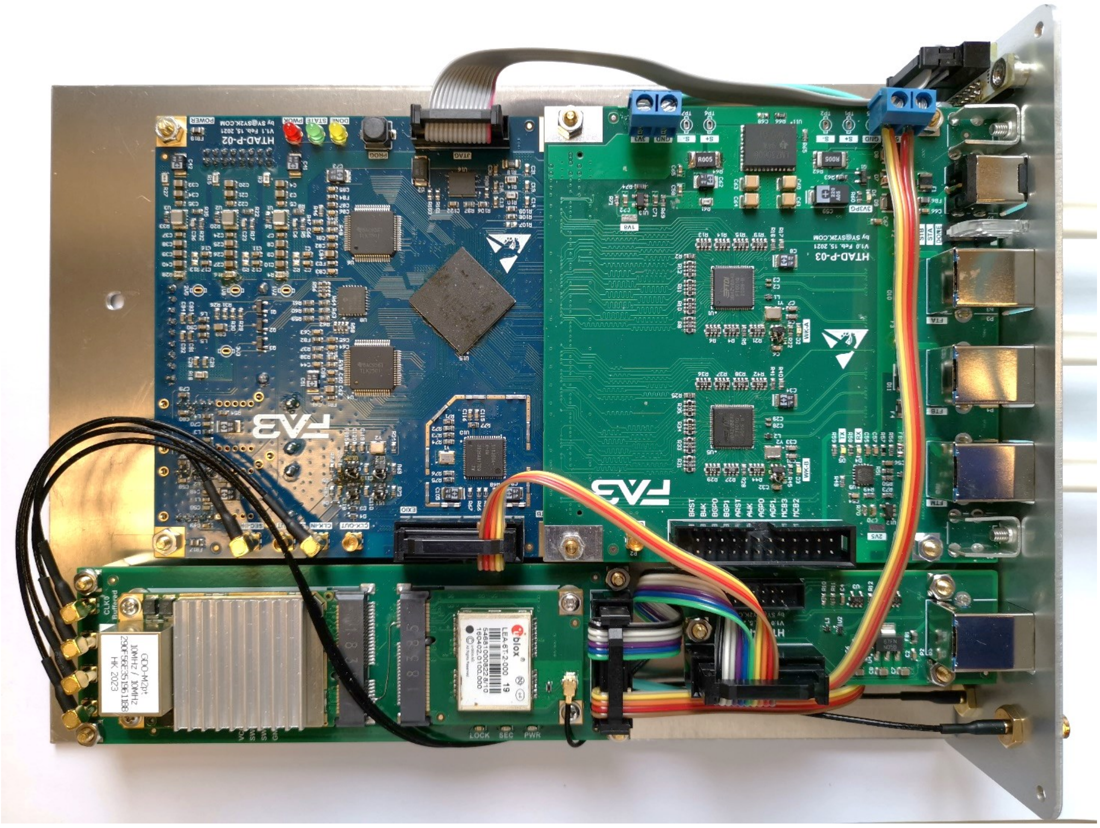

Figure 6-4. The internal composition of optical receiver on ground.

Figure 6-5. The front panel of optical receiver on ground.

6.2. Performance Testing of Analog Front-End in Laboratory

After the lightning current is converted into voltage through the shunt resistor, the attenuator module protects and attenuates the large signal at the first stage of whole acquisition system, and its frequency characteristic has a direct limiting effect on the system bandwidth. **Figure 6-6** shows the frequency and phase characteristics of the attenuator module. It can be seen that both the protection circuit for the high gain channel and the attenuation circuit for the low gain channel have flat frequency characteristics from DC to about 40MHz. And the fluctuations around 42MHz may be caused by the junction capacitance of the protection diode and the stray inductance in the cavity.

In the analog front-end circuit board design, micro-coaxial connectors with switches are inserted between circuit stages to facilitate analog performance testing. By using the connector with switch, the subsequent circuit can be disconnected while the signal is being measured and more accurate results can be obtained. **Figure 6-7** shows the frequency and phase characteristics of four ranges, and **Table 6-1** compares the differences between design specifications and actual circuit characteristics, which can be seen that the implemented circuit parameters are very close to the design values. The gain error mainly comes from the error in the resistor value, which is caused by two reasons. One is the actual resistance value produced according to the E96 series, and the other is the tolerance of the resistance itself. However, the DC gain error is acceptable and easily calibrated rather than the fluctuation on the frequency response.

The higher DC gain error of Range 2 and 3 is mainly due to the use of passive LC filters, where the equivalent series resistance of inductors leads to more signal attenuation.

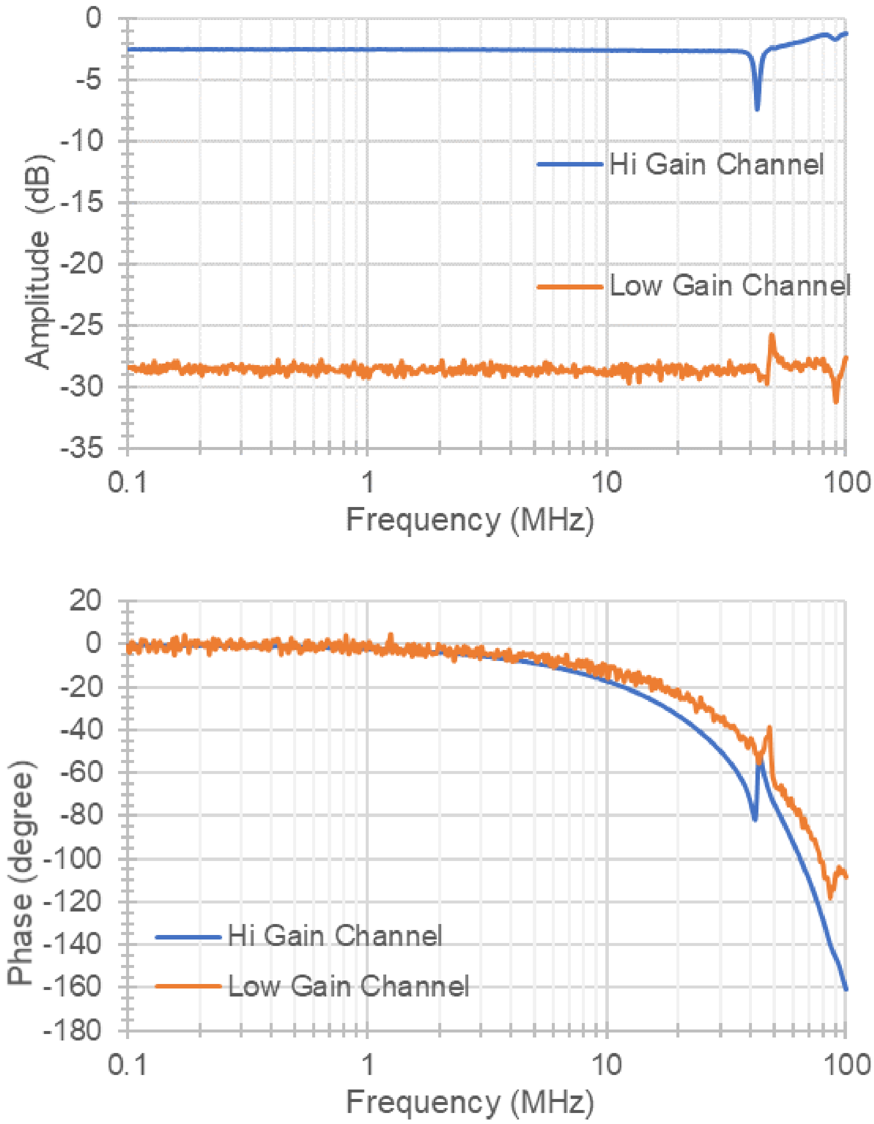

Figure 6-6. The frequency response and output phase of the attenuator.

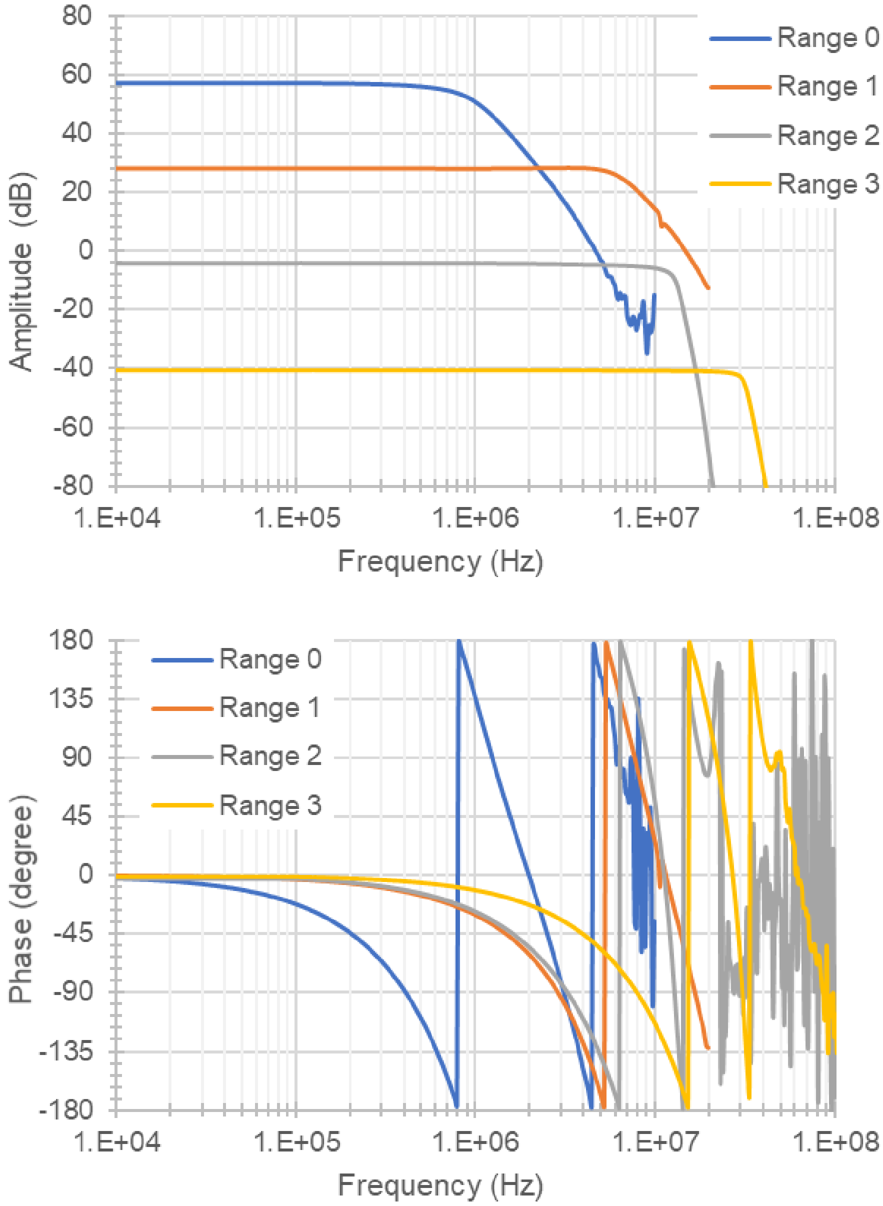

Figure 6-7. The frequency response and output phase of different ranges.

Table 6-1. Summary of the AFE performance of different ranges.

	Range 0	Range 1	Range 2	Range 3
Designed voltage gain	750 V/V	24.90 V/V	0.628 V/V	9.94 mV/V
Actualized voltage gain	742.4 V/V	24.652 V/V	0.6086 V/V	9.576 mV/V
Gain error	− 1.02 %	− 1.00 %	− 3.09 %	− 3.67 %

Designed -3dB bandwidth	> 600 kHz	6.5 MHz	12 MHz	30 MHz
Actualized bandwidth	758 kHz	6.47 MHz	11.7 MHz	30.3 MHz

6.3. Input Surge Tolerance Tests in Laboratory

In this study, two different testing methods were used to determine the surge tolerance capacity of the input protection circuit, and their simplified circuits are shown in **Figure 6-8**. The circuit (a) uses a regulated power supply with a controlled MOSFET to generate 10 ms square pulses up to 25 V and 1 ms square pulses up to 100 V to simulate both the continuous current and impulsive return stroke current in lightning. In circuit (b), an impulse current generator is used in conjunction with a 0.25 mΩ coaxial shunt resistor to effectively emulate the situation when a lightning discharge strikes on the tower, and a maximum peak value of 78 kA with a standard 8/20 μs lightning impulse waveform can be generated.

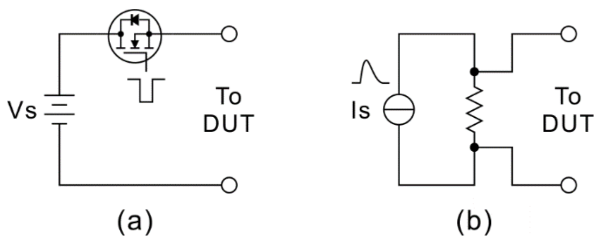

Figure 6-8. Equivalent circuits of two voltage pulse generators: (a) using a regulated power supply and a controlled MOSFET to generate square pulses, and (b) using a pulse current generator with a coaxial shunt resistor to generate a standard 8/20 μs lightning impulse waveform.

Multiple repetitions of each shock type were conducted, and no alterations to the voltage gain and noise performance were observed.

6.4. Software Development Progress

Because the computer software has not been completed, only the transmission interface and the GUI are tested. **Figure 6-9** shows the screenshot of the bit error ratetest. In this test each data packet contains 2048 bytes and is sent through the ground system using the command interface and transmitted back through the optical data link by the tower system. The experimental result is that out of 1,822,959 packets, only two errors are detected, which the error rate is only about 1 part in a million. In addition, the second error occurred after the USB cable was shaken, possibly due to a loose USB connector.

The graphical user interface (GUI) is shown in **Figure 6-10**. In addition to the system initial configuration parameters define in the file, the GUI can effectively view the real-time system status and adjust the working mode. On the left side of the window, the system name, the status of each module, and the computer system status are indicated. In the middle of the window, the waveforms are displayed in the upper area, and the lower part is the settings of serial interfaces and storage locations. At the right side of the window, the trigger mode settings, signal amplitude indication and window zoom settings are arranged. All settings in the window can be saved and recalled for easy use, and locked to prevent misoperation during automatic operation of the system.

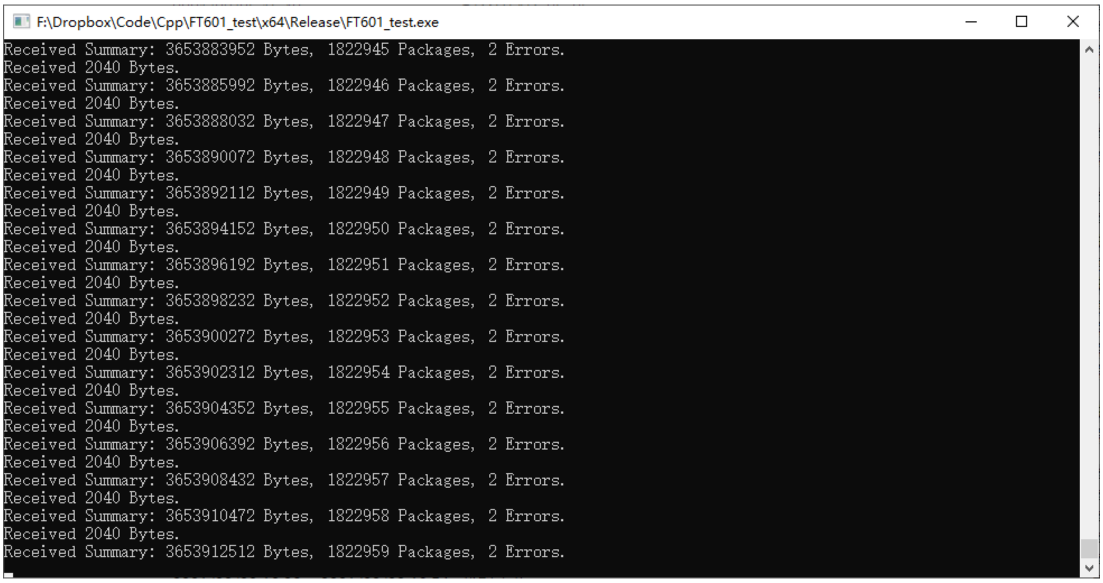

Figure 6-9. Test screenshot of data link bit error rate.

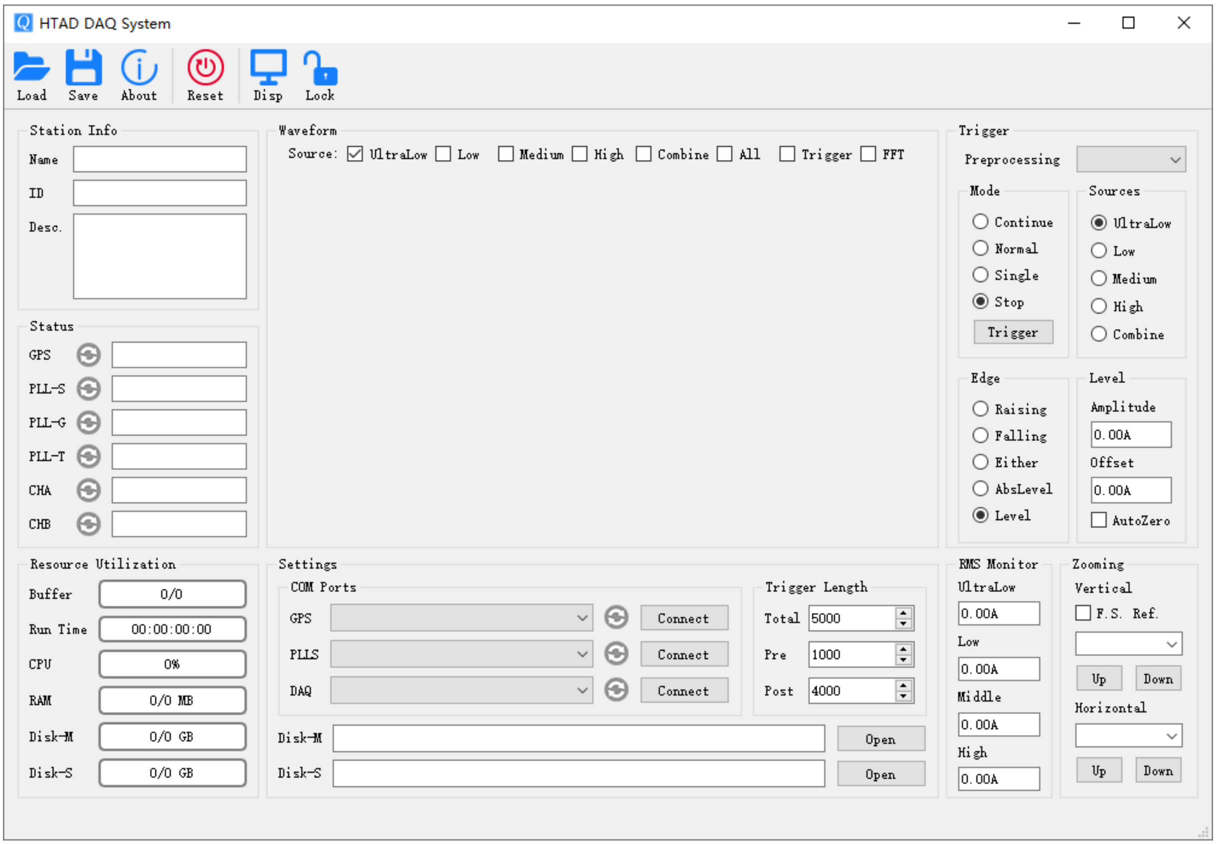

Figure 6-10. Graphical user interface for computer software.

6.5. Conclusion

In this study, the implement of a complete lightning current acquisition system is required rather than architectural design only. Although part of the computer software has not been completed, the hardware and software test results presented in this chapter are close to the expected goals, which have been demonstrated the feasibility of the system design.

Chapter 7. Preliminary Field Observation Results

After assembling and testing in the laboratory, the core component of this multi-range lightning current measurement system, the analog front-end, was first installed and tested via the current shunt on SZMGT to measure milliampere corona discharge current formed at the initial stage of a lightning discharge. And due to limitations of the data acquisition system, only channels 0 and 3 were recorded, marked as high-gain channel (Ch2) and bypass channel (Ch1), respectively.

Due to the strong electromagnetic interference surrounding the observation site, the analog bandwidth of AFE is first reduced and then be compensated in digital domain. Additionally, a specially designed digital filter is added to further improve the signal-to-noise ratio.

7.1. Analog Bandwidth Adjustment and Background Noise Measurement

To avoid output saturation of the high-gain channel caused by the medium wave radio resonance on the tower, the hardware analog bandwidth was first limited, and then compensated in digital domain. The different frequency response curves during the adjustment process are shown in **Figure 7-1**, and the 3 dB bandwidth before and after analog bandwidth limitation and digital compensation are 758 kHz, 225 kHz and 1.58 MHz, respectively.

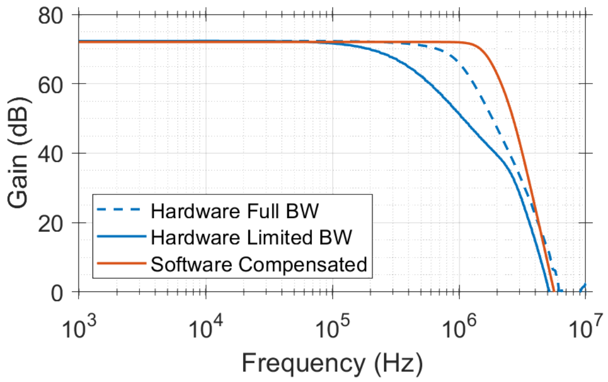

Figure 7-1. Frequency response of the high-gain amplifier, where blue dotted line represents the original full bandwidth of the hardware circuit, blue solid line represents the limited analog bandwidth to prevent output saturation, and the red line represents the software compensated bandwidth in digital domain.

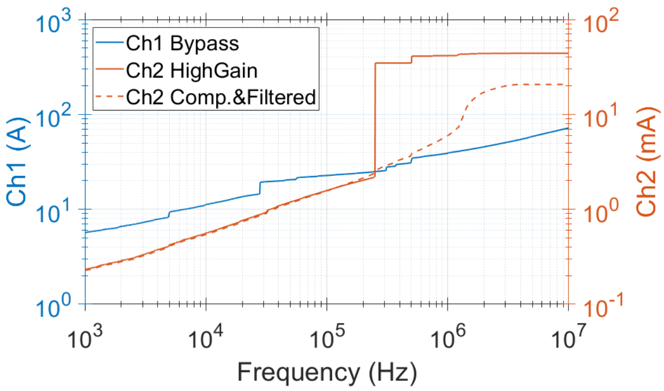

Figure 7-2. Equivalent integral current noise versus bandwidth of the lightning current measurement system, where Ch1 sampled the output voltage of the shunt directly, and Ch2 sampled the high-gain output of the AFE module.

Shown in **Figure 7-2** is the noise performance result of the first test after the AFE module was installed on the tower. Where the blue line represents the bypass channel, and the red lines represent the signal sampled from the high-gain channel before and after digital compensation and filtering. The equivalent current noise floors of these three situations are 70 A, 44 mA and 20 mA, respectively, which indicates a huge improvement on the detection capability after the installation of this AFE with digital signal processing. It should also be noted that the noise with a frequency of 250 kHz and its harmonics was mainly generated by the power supply system on the tower, which interfered with the measurement system through line couplings.

7.2. Digital Frequency Response Compensation and Filtering

As the application site of the AFE designed is situated near a medium-wave transmission station, and the 356 m high steel tower exhibits significant coupling with the frequency range spanning from 0.2 MHz to 10 MHz, previous experiments had shown that the preamplifier output was saturated upon installation on top of the tower. In addition, because there are many frequencies of medium-wave signals, it is very difficult to configure a hardware notch filter for each signal. Therefore, in this study, the hardware high-frequency gain is first limited to avoid signal saturation, and then a software algorithm is used to compensate the frequency response and filter the radio signals.

7.2.1. Digital Frequency Response Compensation

To compensate the frequency response of the circuit after bandwidth limitation, first, both the hardware frequency response given by equation (7-1) and the desired frequency response described by equation (7-2) are established. Then, the Fourier and inverse Fourier transforms in equation (7-3) are used to process the collected current data sequence.

$$H_H(j\omega) = H_H(s)|_{s=j\omega} = \\ A \cdot \frac{\omega_1^2}{s^2+2\zeta_1\omega_1 \cdot s+\omega_1^2)} \cdot \frac{\omega_2^2}{s^2+2\zeta_2\omega_2 \cdot s+\omega_2^2)} \cdot \frac{\omega_3^2}{s^2+2\zeta_3\omega_3 \cdot s+\omega_3^2)}\Bigg|_{s=j\omega} \tag{7-1}$$

$$H_C(j\omega) = H_C(s)|_{s=j\omega} = \\ A \cdot \frac{1}{1+p_1 s+p_2 s^2+p_3 s^3+p_4 s^4} \cdot \frac{1}{1+p'_1 s+p'_2 s^2+p'_3 s^3+p'_4 s^4}\Bigg|_{s=j\omega} \tag{7-2}$$

$$f_c(t) = \mathcal{F}^{-1}\left\{\mathcal{F}[f_0(t)] \cdot \frac{H_C(j\omega)}{H_H(j\omega)}\right\} \tag{7-3}$$

For the hardware frequency response, equation (7-1) is proposed to fit the measured results and simplify calculations with different frequency sequences, where ω_1, ω_2 and ω_3 are the corner frequencies of the lower limitation frequency, the original hardware bandwidth and the compensation frequency of op-amp, respectively, and ζ_1, ζ_2 and ζ_3 are their corresponding damping factors. In the present application, two separate first-order RC low-pass filters are used instead of second-order low-pass filters to achieve a smoother frequency response variation and facilitate the frequency compensation, which implies that $\zeta_1 = \zeta_2 = 1$.

In addition, two 4th-order Butterworth low-pass filters with different corner frequencies are used to construct the desired frequency response, which the filter with a lower corner frequency is used to limit the maximum gain provided by the software compensation, and the filter with a higher corner frequency is used to suppress high frequency noises. The transfer function of the desired frequency response is as shown by equation (7-2), where the details and calculation methods of all the parameters are referring to (Analog Devices Incorporated, 2008).

7.2.2. Digital Filtering

In order to improve further the system sensitivity and observation data quality, a multi-frequency notch filter is designed to address the narrowband interference signals found in the noise measurement between 700 kHz and 10 MHz. The identification of noise frequencies is done by comparing the noise spectrum measured on a sunny day with the signal spectrum of the observed lightning current waveform under thunderstorm, as shown in **Figure 7-3**. Multiple narrowband interference signals with the same frequency can be easily detected between two spectrums. However, since the occurrence and intensity of these interference signals may vary over time, an identification threshold is set starting from 200 kHz (indicated by the red line in **Figure 7-3**). Any signal that exceeds the threshold and has a bandwidth narrower than 0.002 times the center frequency is considered as interference, which will be removed by inserting a notch filter with a bandwidth of 0.004 times the center frequency of the signal.

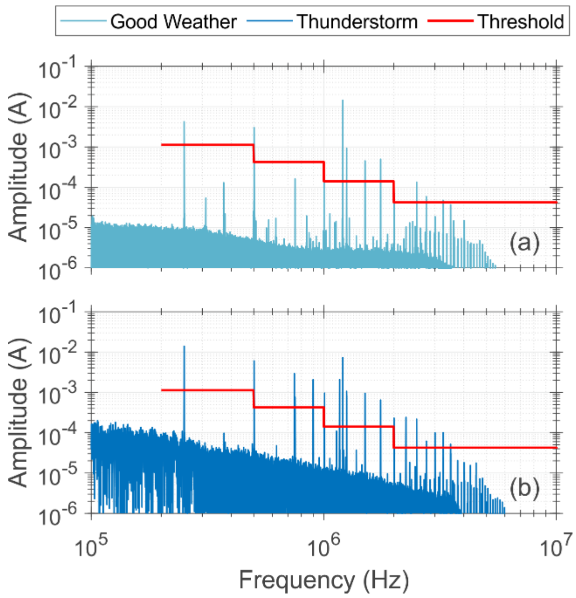

Figure 7-3. Comparisons of the noise spectrum measured on a sunny day (a) with the signal spectrum of the observed lightning current waveform (b), and the identification thresholds for the frequencies of the inserted notch filter (red line).

For choosing the digital filter, different types and orders of digital notch filters are attempted, including the commonly used Butterworth, Chebyshev, and elliptic filters. However, finding a balance between the effectivity of noise suppression and the impulse response shown on the output waveforms always be difficult due to the large number of filters with different frequencies that are required. At the end, the method of zeroing out bins of FFT is attempted and performs well in both aspects.

The zeroing out bins of FFT method first performs a Fast Fourier Transform (FFT) on the original signal to convert it to the digital domain, then zeros the FFT bins within the bandwidth of 0.004 times the center frequency of each interference signal, and performs an Inverse Fast Fourier Transform (IFFT) to convert the signal back to the time domain. This method is not usually recommended because it produces a sinc-like impulse response that extends to infinite time in both directions (Oppenheim & Schafer, 2009), which is also known as the Gibbs phenomenon (Nahin, 2011). It also has a higher computational complexity of O(NlogN) (Duhamel & Vetterli, 1990) compared to O(N) for FIR and IIR filters (Williams & Taylor, 2006), making it less suitable for real-time signal processing than other digital filters. However, this approach can be accepted when the following three points are met: i) the frequency band to be filtered out is considered to contain no valid signal, ii) the same length data is used for both FFT and IFFT operations, and iii) the output waveform is carefully checked. In this case, as the interference signals to be filtered out have a narrow bandwidth and lightning currents have a wideband characteristic (Uman & Krider, 1982), it can be approximated that removing these narrowband frequencies will not have a significant impact on the original signal. In addition, because the lightning current observation system uses a trigger-storage-analysis processing flow, which has a lower real-time signal processing requirement and a higher tolerance for computational complexity. More importantly, the output waveform obtained using this method, shown in **Figure 7-4**, does not exhibit any negative issues such as oscillation, which suggests that the use of this method is successful in this application.

In **Figure 7-4** the upper panel compares the raw data with the filtered data from the high-gain output under low signal conditions. Weaker current pulses with amplitudes between 50 mA and 200 mA can be identified in the filtered waveform, indicating a significant improvement in system sensitivity and data quality. The lower panel also compares the difference before and after filter processing under the condition with large pulses, but little difference can be found, demonstrating the high reliability of the filter method.

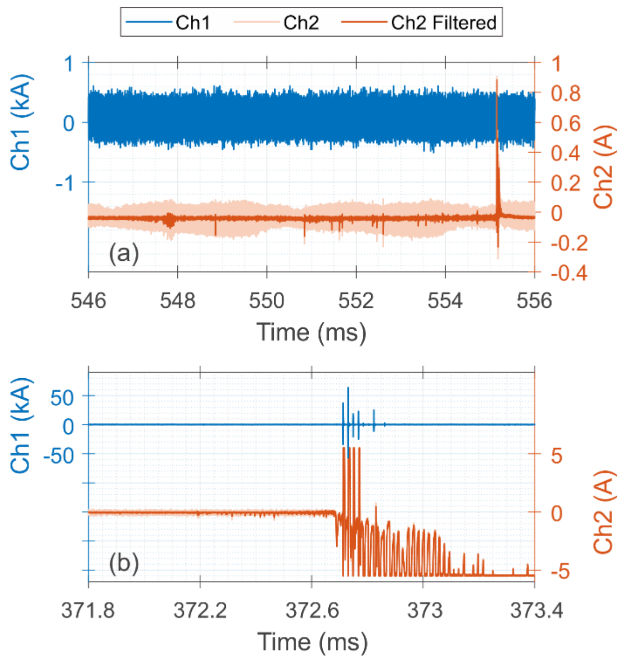

Figure 7-4. Details of observed lightning current waveform before and after filtering with the targeted multi-frequency notch filter, where Ch1 is the bypass channel and the Ch2 is the high-gain output channel.

7.3. Preliminary Results of Corona Discharge Current Measurements

With the AFE on SZMGT, we have successfully recorded two sets of lightning currents ranging from several tens of mill-amps to hundreds of kilo-amps. Waveforms and details of the lightning currents recorded and those after noise filtering and compensation (the light orange ones) are shown in **Figure 7-5** and **Figure 7-6**. It is obvious that those with noise compensation provide more high-frequency details of the corona discharge phenomenon.

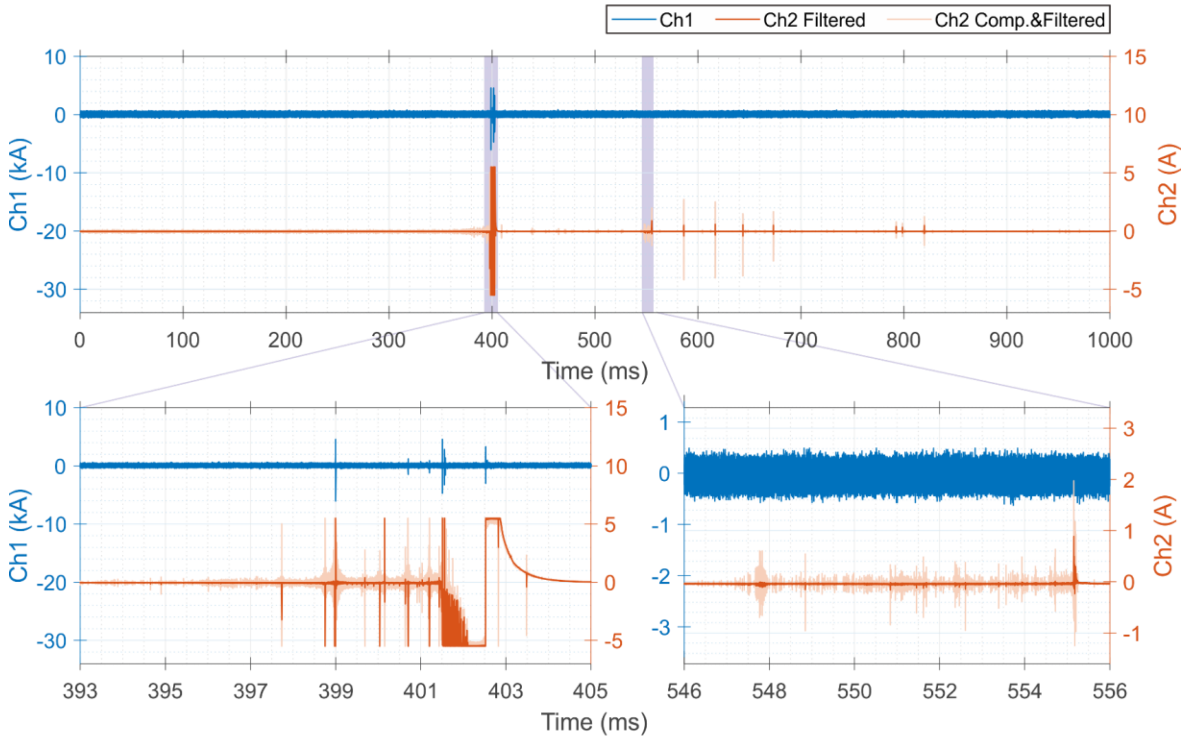

Figure 7-5. The current waveform recorded from very initial stages of lightning event on Sep. 15, 2019 with a peak current of -6.0 kA.

Figure 7-5 shows the current waveform of an unconnected upward positive leader process occurred on Sep. 15, 2019 with a peak current of -6.0 kA. From the high gain channel (Ch2), the continuous development of the upward leader occurred at the time around 401 ms and ended about 1 ms after that time. Whilst the bypass channel (Ch1) only captured individual short pulse oscillations, which might be caused by the tower resonance. Furthermore, the corona discharge with peak currents of tens of milliamperes were found from the beginning of the current recording on the high-gain channel, and both the peak value and occurrence frequency of the corona discharge showed an increase after the time 395.8 ms, which showed the correlation with the development of lightning leader channel.

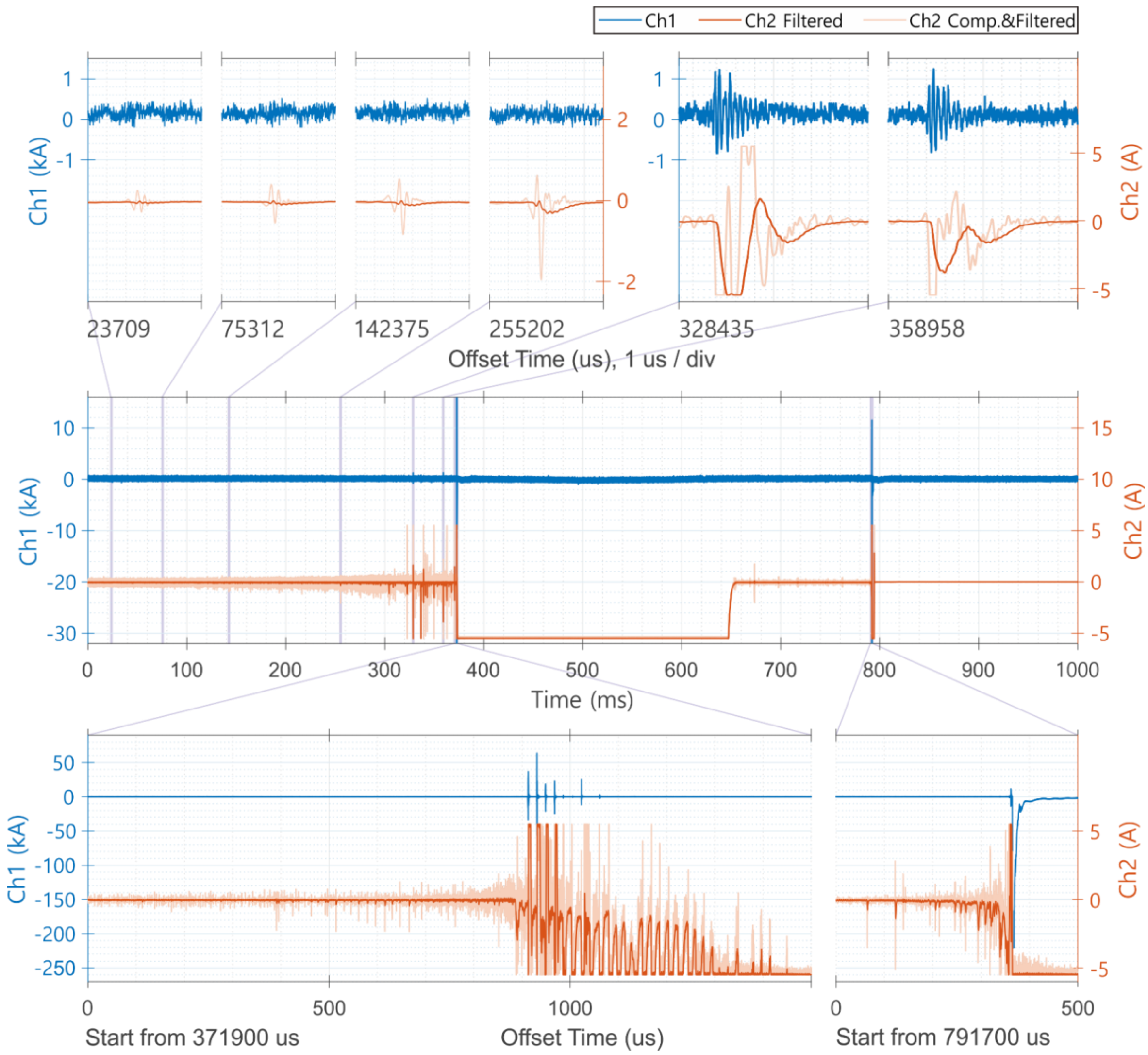

Figure 7-6. The current waveform recorded from very initial stages of lightning event on May 30, 2020 with the return stroke peak current exceeding -220 kA. Please note that after 792.5 ms, the signal of second E/O channel was interrupted.

Figure 7-6 shows the current waveform in a two leader-return-stroke lightning discharge occurred on May 30, 2020, of which the maximum return stroke peak current exceeded -220 kA. In this case, even 300 ms before the continuous development of the upward leader preceding the first return stroke, the corona discharge current peak had reached 340 mA, and then increased continuously. Around 372.8 ms (zoom in on the lower left corner), a series of comb pulses were seen on the high gain channel, which, by referring to current waveforms in (Visacro et al., 2017), could be considered as the continuous development of the lightning leader preceding the first return stroke. At the time around 792.1 ms (zoom in on the lower right corner), the transition from the corona discharge stage to the upward leader preceding the second return stroke showed an noticeable speedup compared to that in the first return stroke process, which may be attributed to the residual channel of the first return stroke process.

7.4. Conclusion

In this section, the background noise of the lightning current observation system on SZMGT, equipped with a shock-tolerated low-noise AFE, was measured and analyzed. A noise floor of 5 μV with an equivalent current of 20 mA on a 0.25 mΩ shunt was achieved from the high-gain channel, indicating a significant improvement in noise reduction. During testing, many narrowband interferences with frequencies between 700 kHz and 10 MHz were detected, and the method of zeroing out bins of FFT was found to be more effective and stable than other digital filter building methods. The measured lightning current waveforms from two lightning events occurred in 2019 and 2020 were also presented, from which the stability and the shock tolerance capacity of the current measuring system were verified. With the digital filter built, an identification amplitude of corona pulse current of around 50 mA was achieved from the output of the high-gain amplifier module. This value is much lower than the detectable level of approximately 300 mA in the raw data of the high-gain output, as well as the 0.5 kA before the installation of the amplifier module.

All of these evidences confirm that this multi-range low-noise lightning current measurement system in combination with a targeted design digital filter can collect valuable lightning current data even in complex electromagnetic interference environments.

Chapter 8. Conclusion and Future Works

In this chapter, the previous work is first summarized. Then, the future works aimed at increasing system integrity will be listed.

8.1. Conclusion

In this study, a multi-range lightning current measurement system with a wide dynamic range from milli-amps to hundreds of kilo-amps was developed and tested on SZMGT to expand the dynamic range of the lightning current measurement. For the first time, this device has enabled the continuous current recording of the whole development process of a lightning discharge to a tall tower, ranging from corona discharge current pulses of tens of milli-amps to lightning return stroke currents of hundreds of kilo-amps. This will definitely benefit the lightning research society for the study of transition from a corona discharge stage to a leader process stage, which is essential for understanding the mechanism of lightning initiation from a tall-grounded object.

To better understand the current gaps in lightning research and propose solutions, the basic process of lightning development, methods for lightning current measurement, and available low-noise techniques in detectors are introduced in Chapter 2. Following the overall framework, analog circuit design, and digital logic design introduced in Chapters 3, 4, and 5, preliminary testing in the laboratory presented in Chapter 6 validated that the basic parameters of this device meet the design requirements.

In Chapter 7, the effectiveness of the analog front-end, which is the core of this equipment and the most difficult to design, as well as related processing algorithms, is verified through the observation of two lightning events. It is shown that the analog front-end, when combined with a low-noise INA, has the capability of measuring currents lower than several milliamps on a 0.25 mΩ shunt, while also being able to withstand lightning current pulses of up to 400 kA. By combining the hardware frequency response adjustment with an adequate digital signal processing algorithm, the problem of analog signal output saturation caused by strong electromagnetic interferences is avoided. Meanwhile, the measurement bandwidth is expanded, and the detection capability for weak signals is further improved. With this combination, an equivalent current noise floor of 20 mA is finally achieved, which is lower than the raw data noise floor of 44 mA from the high-gain output, as well as the 70 A before the installation of the AFE.

8.2. Further Work Arrangements

To further improve the system integrity and make this equipment easier to use, there is still a lot of work that needs to be done to increase the speed of data transmission in optical fibers, as well as improve the convenience of the data acquisition software. More importantly, we have also been attempting to establish a physics model to explain the transition process from corona discharge to leader development during the initial stage of lightning occurrence, and we hope that this research can advance the understanding of the mechanisms behind the initiation of lightning.

References

Aleksandrov, N., Bazelyan, E., & Raizer, Y. (2005). The effect of a corona discharge on a lightning attachment. *Plasma Physics Reports*, *31*, 75–91. https://doi.org/10.1134/1.1856709

Analog Devices Incorporated. (2008). Chapter 8 Analog filters. In *Linear circuit design handbook*.

Analog Devices Incorporated. (2018). *ADA4177 Datasheet*. https://www.analog.com/media/en/technical-documentation/data-sheets/ada4177-1_4177-2_4177-4.pdf

Apex Microtechnology. (2017). *AN53 External Current Limit for Apex Power Op Amps*. https://www.apexanalog.com/resources/appnotes/an53.pdf

Au, H.-A. (1972). *Parameters of the Super-beta Transistor*.

Bazelyan, E. M., Raizer, Y. P., & Aleksandrov, N. L. (2008). Corona initiated from grounded objects under thunderstorm conditions and its influence on lightning attachment. *Plasma Sources Science and Technology*, *17*(2), 024015. https://doi.org/10.1088/0963-0252/17/2/024015

Bejleri, M., Rakov, V. A., Uman, M. A., Rambo, K. J., Mata, C. T., & Fernandez, M. I. (2004). Triggered lightning testing of an airport runway lighting system. *IEEE Transactions on Electromagnetic Compatibility*, *46*(1), 96–101.

Berger, K. (1967). Novel Observations on Lightning Discharges: Results ofResearch on Mount San Salvatore. *J. Franklin Inst*, *283*, 478–525.

Berger, K. (1975). Parameters of lightning flashes. *Electra*, *41*, 23–37.

Berger, K., & Vogelsanger, E. (1969). New results of lightning observations. *Planetary Electrodynamics*, *1*, 489–510.

Biagi, C. J., Jordan, D. M., Uman, M. A., Hill, J. D., Beasley, W. H., & Howard, J. (2009). High-speed video observations of rocket-and-wire initiated lightning. *Geophysical Research Letters*, *36*(15).

Brook, M., Armstrong, G., Winder, R. P. H., Vonnegut, B., & Moore, C. B. (1961). Artificial initiation of lightning discharges. *Journal of Geophysical Research*, *66*(11), 3967–3969. https://doi.org/10.1029/JZ066i011p03967

Bruce, C. E. R., & Golde, R. H. (1941). The lightning discharge. *Journal of the Institution of Electrical Engineers-Part II: Power Engineering*, *88*(6), 487–505.

Burke, H. K., & Few, A. A. (1978). Direct measurements of the atmospheric conduction current. *Journal of Geophysical Research: Oceans*, *83*(C6), 3093–3098.

Chowdhuri, P., Anderson, J. G., Chisholm, W. A., Field, T. E., Ishii, M., Martinez, J. A., Marz, M. B., McDaniel, J., McDermott, T. E., & Mousa, A. M. (2005). Parameters of lightning strokes: A review. *IEEE Transactions on Power Delivery*, *20*(1), 346–358.

Christian, H. J. (2003). Global frequency and distribution of lightning as observed from space by the Optical Transient Detector. *Journal of Geophysical Research*, *108*(D1). https://doi.org/10.1029/2002jd002347

D'Alessandro, F. (2009). Experimental study of the effect of wind on positive and negative corona from a sharp point in a thunderstorm. *Journal of Electrostatics*, *67*(2), 482–487. https://doi.org/10.1016/j.elstat.2008.12.003

Das, S., & Kumar, U. (2022). Modeling of Bi-Polar Leader Inception and Propagation from Flying Aircraft Prior to a Lightning Strike. *Atmosphere*, *13*(6), 943.

Day, C. C., & Holte, B. (1971). *Two-terminal bipolar self-powered low current limiter* (Patent No. US3603811A). https://patents.google.com/patent/US3603811A

Dellera, L., Garbagnati, E., LaPiparo, G., Ronchetti, P., & Solbiati, G. (1985). Lightning Protection of Structures Part I: Lightning Current Parameters. *Report of Working Group of Italian Electrotechnical Committee, Technical Committee 81*, 15.

Diendorfer, G., Pichler, H., & Mair, M. (2009). Some parameters of negative upward-initiated lightning to the Gaisberg tower (2000–2007). *IEEE Transactions on Electromagnetic Compatibility*, *51*(3), 443–452.

Diendorfer, G., Zhou, H., & Pichler, H. (2011). *Review of 10 years of lightning measurement at the Gaisberg Tower in Austria*. Proc. 3rd Int. Symposium on Winter Lightning (ISWL), Sapporo, Japan.

Drung, D., & Storm, J.-H. (2011). Ultralow-noise chopper amplifier with low input charge injection. *IEEE Transactions on Instrumentation and Measurement*, *60*(7), 2347–2352.

Duhamel, P., & Vetterli, M. (1990). Fast Fourier transforms: A tutorial review and a state of the art. *Signal Processing*, *19*(4), 259–299.

Fieux, R. P., Gary, C. H., & Hubert, P. L. (1975). Artificially triggered lightning above land. *Nature*, *257*(5523), 212–214.

Fieux, R. P., Gary, C. H., Hutzler, B. P., Eybert-Berard, A. R., Hubert, P. L., Meesters, A. C., Perroud, P. H., Hamelin, J. H., & Person, J. M. (1978). Research on Artificiallyu Triggered Lightning in France. *IEEE Transactions on Power Apparatus and Systems*, *3*, 725–733.

Fisher, R. J., Schnetzer, G. H., Thottappillil, R., Rakov, V. A., Uman, M. A., & Goldberg, J. D. (1993). Parameters of triggered-lightning flashes in Florida and Alabama. *Journal of Geophysical Research: Atmospheres*, *98*(D12), 22887–22902.

Gallimberti, I. (1979). The mechanism of the long spark formation. *Le Journal de Physique Colloques*, *40*(C7), C7-193-C7-250.

Gao, L., Larsson, A., & Cooray, V. (2000). Simulation of streamer discharges as finitely conducting channels [comments and reply]. *IEEE Transactions on Dielectrics and Electrical Insulation*, *7*(3), 458–460.

Gijben, M. (2012). The lightning climatology of South Africa. *South African Journal of Science*, *108*(3), 1–10.

Golde, R. H. (1978). *Lightning and tall structures*. *125*, 347–351.

Gorin, B. N. (1984). Measurements of lightning currents at the Ostankino tower. *Electrichestrvo*, *8*, 64–65.

Gorin, B. N., Levitov, V. I., & Shkilev, A. V. (1976). *Some principles of leader discharge of air gaps with a strong non-uniform field*. *143*, 274–278.

Gruchalla, M. E. (2008). *CURRENT-VIEWING RESISTOR VALIDATION AND APPLICATION*. http://www.ib-billmann.de/bilder/pdf/05_CVRAnalysys-Rev7.pdf

Harris, H. F., & Smith, T. E. (1957). Low level transistorized chopper amplifier. *IRE Transactions on Telemetry and Remote Control*, *1*, 1–8.

Heidler, F. H., Manhardt, M., & Stimper, K. (2014). Characteristics of upward positive lightning initiated from the Peissenberg Tower, Germany. *IEEE Transactions on Electromagnetic Compatibility*, *57*(1), 102–111.

Horii, K. (1982). Experiment of artificial lightning triggered with rocket. *Nagoya Univ. Mem. of the Fac. of Eng., Nagoya Univ.*, *34*(1), 77–112.

Hu, C. (1979). Optimum doping profile for minimum ohmic resistance and high-breakdown voltage. *IEEE Transactions on Electron Devices*, *26*(3), 243–244.

Hussein, A. M., Janischewskyj, W., Milewski, M., Shostak, V., Chisholm, W., & Chang, J. S. (2004). Current waveform parameters of CN tower lightning return strokes. *Journal of Electrostatics*, *60*(2), 149–162. https://doi.org/10.1016/j.elstat.2004.01.002

Idone, V. P., & Orville, R. E. (1984). Three unusual strokes in a triggered lightning flash. *Journal of Geophysical Research: Atmospheres*, *89*(D5), 7311–7316.

Idone, V. P., Orville, R. E., Hubert, P., Barret, L., & Eybert-Berard, A. (1984). Correlated observations of three triggered lightning flashes. *Journal of Geophysical Research: Atmospheres*, *89*(D1), 1385–1394.

Igoe, L. T. (2016). Capturing "Jove's Autograph": Late Nineteenth-Century Lightning Photography and Electrical Agency. *Panorama: Journal of the Association of Historians of American Art*, *2 no. 1 (Summer, 2016)*. https://doi.org/10.24926/24716839.1535

InterFET Corporation. (2019). *IF9030 Datasheet*. https://www.interfet.com/jfet-datasheets/jfet-if9030-interfet.pdf

InterFET Corporation. (2022). *IF3602 Datasheet*. https://www.interfet.com/jfet-datasheets/jfet-if3602-interfet.pdf

J. Takami, & S. Okabe. (2007). Observational Results of Lightning Current on Transmission Towers. *IEEE Transactions on Power Delivery*, *22*(1), 547–556. https://doi.org/10.1109/TPWRD.2006.883006

Janischewskyj, W., Hussein, A. M., Shostak, V., Rusan, I., Li, J.-X., & Chang, J.-S. (1997). Statistics of lightning strikes to the Toronto Canadian National Tower (1978-1995). *IEEE Transactions on Power Delivery*, *12*(3), 1210–1221.

Jiang, R., Qie, X., Wang, C., & Yang, J. (2013). Propagating features of upward positive leaders in the initial stage of rocket-triggered lightning. *Atmospheric Research*, *129*, 90–96.

Kitchin, C., & Counts, L. (2006). *A designer's guide to instrumentation amplifiers*.

Analog Devices Norwood, MA.

Kong, X., Qie, X., & Zhao, Y. (2008). Characteristics of downward leader in a positive cloud-to-ground lightning flash observed by high-speed video camera and electric field changes. *Geophysical Research Letters*, *35*(5).

Krider, E. P., & Radda, G. J. (1975). Radiation field wave forms produced by lightning stepped leaders. *Journal of Geophysical Research*, *80*(18), 2653–2657.

Krider, E. P., Weidman, C. D., & Noggle, R. C. (1977). The electric fields produced by lightning stepped leaders. *Journal of Geophysical Research*, *82*(6), 951–960.

Lalande, P., Bondiou-Clergerie, A., Laroche, P., Eybert-Berard, A., Berlandis, J.-P., Bador, B., Bonamy, A., Uman, M. A., & Rakov, V. A. (1998). Leader properties determined with triggered lightning techniques. *Journal of Geophysical Research: Atmospheres*, *103*(D12), 14109–14115.

Le Boulch, M., & Plantier, T. (1990). *The Meteorage thunderstorm monitoring system: A tool for new EMC protection strategies*. Proc. 20th Int. Conf. on Lightning Protection.

Leach, W. M. (1994). Fundamentals of low-noise analog circuit design. *Proceedings of the IEEE*, *82*(10), 1515–1538.

Lei, J., & Calif, M. (1998). *High voltage current limiting protection circuit and method therefor* (Patent No. US5729418A). https://patents.google.com/patent/US5729418A

Levinzon, F. A. (2005). Measurement of low-frequency noise of modern low-noise junction field effect transistors. *IEEE Transactions on Instrumentation and Measurement*, *54*(6), 2427–2432.

Levinzon, F. A., & Vandamme, L. K. J. (2011). Comparison of 1/f noise in JFETs and MOSFETs with several figures of merit. *Fluctuation and Noise Letters*, *10*(04), 447–465.

Li, J., Xi, Z., Chen, X., Wang, H., Long, X., Zhou, S., & Wang, L. (2020). Ultralow Noise Low Offset Chopper Amplifier for Induction Coil Sensor to Detect Geomagnetic Field of 1 mHz to 1 kHz. *Journal of Environmental and Engineering Geophysics*, *25*(4), 497–511.

Li, Z., Zhang, Q., Zhang, L., Liu, F., & Tan, X. (2011). Design of Rogowski Coil with external integrator for measurement of lightning current up to 400kA. *Przeglad Elektrotechniczny*, *87*, 188–192.

Loeb, L. B. (1966). The mechanisms of stepped and dart leaders in cloud-to-ground lightning strokes. *Journal of Geophysical Research*, *71*(20), 4711–4721.

Loeb, L. B. (2022). *Electrical coronas: Their basic physical mechanisms*. Univ of California Press.

Manoochehrnia, P., Schulz, W., Rachidi, F., & Rubinstein, M. (2008). *Lightning statistics in the regions of Saentis and St. Chrischona towers in Switzerland*. *1*, 2–3.

Marlton, G., Harrison, R. G., & Nicoll, K. A. (2013). *Atmospheric Point Discharge Currents measured with a bi-polar logarithmic current amplifier*. EPSC2013-181.

McEachron, K. B. (1938). Lightning to the empire state building. *Electrical Engineering*, *57*(12), 493–505.

McEachron, K. B. (1941). Lightning to the empire state building. *Transactions of the American Institute of Electrical Engineers*, *60*(9), 885–890.

Miki, M., Miki, T., Asakawa, A., & Shindo, T. (2014). *Characteristics of negative upward stepped leaders in positive upward lightning*. XV International Conference on Atmospheric Electricity.

Miki, M., Rakov, V. A., Shindo, T., Diendorfer, G., Mair, M., Heidler, F., Zischank, W., Uman, M. A., Thottappillil, R., & Wang, D. (2005). Initial stage in lightning initiated from tall objects and in rocket-triggered lightning. *Journal of Geophysical Research: Atmospheres*, *110*(D2).

Moghimi, R. (2010). *Low noise signal conditioning for sensor-based circuits*. Analog Devices, Inc.

Moore, C. B., Aulich, G. D., & Rison, W. (2000). Measurements of lightning rod responses to nearby strikes. *Geophysical Research Letters*, *27*(10), 1487–1490. https://doi.org/10.1029/1999GL011053

Nahin, P. J. (2011). *Dr. Euler's Fabulous Formula: Cures Many Mathematical Ills* (Vol. 52). Princeton University Press.

Narita, K., Goto, Y., Komuro, H., & Sawada, S. (1989). Bipolar lightning in winter at Maki, Japan. *Journal of Geophysical Research: Atmospheres*, *94*(D11), 13191–

13195.

Newman, M. M., Stahmann, J. R., Robb, J. D., Lewis, E. A., Martin, S. G., & Zinn, S. V. (1967). Triggered lightning strokes at very close range. *Journal of Geophysical Research*, *72*(18), 4761–4764.

Oppenheim, A. V., & Schafer, R. W. (2009). *Discrete-Time Signal Processing* (3rd ed.). Prentice Hall Press.

Pierce, E. T. (1955). The development of lightning discharges. *Quarterly Journal of the Royal Meteorological Society*, *81*(348), 229–240.

Pierce, E. T. (1972). *Triggered lightning and some unsuspected lightning hazards*. STANFORD RESEARCH INST MENLO PARK CA.

Qie, X., Zhang, Q., Zhou, Y., Feng, G., Zhang, T., Yang, J., Kong, X., Xiao, Q., & Wu, S. (2007). Artificially triggered lightning and its characteristic discharge parameters in two severe thunderstorms. *Science in China Series D: Earth Sciences*, *50*(8), 1241–1250.

Raizer, Y. P., & Allen, J. E. (1991). *Gas discharge physics* (Vol. 1). Springer.

Rakov, V. A. (2003). A review of the interaction of lightning with tall objects. *Recent Res. Develop. Geophys*, *5*, 57–71.

Rakov, V. A., & Uman, M. A. (2003). *Lightning: Physics and Effects*. Cambridge university press.

Rakov, V. A., Uman, M. A., Fernandez, M. I., Mata, C. T., Rambo, K. J., Stapleton, M. V., & Sutil, R. R. (2002). Direct lightning strikes to the lightning protective system of a residential building: Triggered-lightning experiments. *IEEE Transactions on Power Delivery*, *17*(2), 575–586.

Romero, C., Paolone, M., Rubinstein, M., Rachidi, F., Rubinstein, A., Diendorfer, G., Schulz, W., Daout, B., Kälin, A., & Zweiacker, P. (2012). A system for the measurements of lightning currents at the Säntis Tower. *Electric Power Systems Research*, *82*(1), 34–43.

Romero, C., Rachidi, F., Rubinstein, M., Paolone, M., Rakov, V. A., & Pavanello, D. (2013). Positive lightning flashes recorded on the Säntis tower from May 2010 to January 2012. *Journal of Geophysical Research: Atmospheres*, *118*(23), 12,879-12,892.

Schonland, B. F. J., Malan, D. J., & Collens, H. (1935). Progressive lightning—II. *Proceedings of the Royal Society of London. Series A-Mathematical and Physical Sciences*, *152*(877), 595–625.

Schröder, D., & Weinhausen, G. (1979). Calculation of thermal noise in JFETs. *IEE Journal on Solid-State and Electron Devices*, *3*(5), 137–141.

Stekolnikov, I., & Valeev, C. (1937). *L'Etude de la Foudre dans un Laboratoire de Campagne*. International Conference on Large High-Voltage Systems (CIGRE).

Texas Instruments Incorporated. (2019). *INA818 Datasheet*. https://www.ti.com/lit/ds/symlink/ina818.pdf

Texas Instruments Incorporated. (2021). *INA849 Datasheet*. https://www.ti.com/lit/ds/symlink/ina849.pdf

Texas Instruments Incorporated. (2022). *INA118 Datasheet*. https://www.ti.com/lit/ds/symlink/ina118.pdf

THAT Corporation. (2013). *THAT 300 Series Datasheet*. https://www.thatcorp.com/datashts/THAT_300-Series_Datasheet.pdf

Uman, M. A. (2001). *The lightning discharge*. Courier Corporation.

Uman, M. A., & Krider, E. P. (1982). A review of natural lightning: Experimental data and modeling. *IEEE Transactions on Electromagnetic Compatibility*, *2*, 79–112.

Uman, M. A., Orville, R. E., & Salanave, L. E. (1964). The density, pressure, and particle distribution in a lightning stroke near peak temperature. *Journal of Atmospheric Sciences*, *21*(3), 306–310.

Visacro, S., Guimaraes, M., & Murta Vale, M. H. (2017). Features of Upward Positive Leaders Initiated From Towers in Natural Cloud-to-Ground Lightning Based on Simultaneous High-Speed Videos, Measured Currents, and Electric Fields. *Journal of Geophysical Research: Atmospheres*, *122*(23), 12,786-12,800. https://doi.org/10.1002/2017JD027016

Visacro, S., Mesquita, C. R., De Conti, A., & Silveira, F. H. (2012). Updated statistics of lightning currents measured at Morro do Cachimbo Station. *Atmospheric Research*, *117*, 55–63.

Visacro, S., Soares Jr, A., Schroeder, M. A. O., Cherchiglia, L. C., & de Sousa, V. J. (2004). Statistical analysis of lightning current parameters: Measurements at

Morro do Cachimbo Station. *Journal of Geophysical Research: Atmospheres*, *109*(D1).

Wada, A., Miki, M., & Asakawa, A. (2004). *Upward Lightning Flashes Observed at the 200-m Fukui Chimney in Winter*. *2004*, AE41A-06.

Wang, D., Takagi, N., Watanabe, T., Sakurano, H., & Hashimoto, M. (2008). Observed characteristics of upward leaders that are initiated from a windmill and its lightning protection tower. *Geophysical Research Letters*, *35*(2).

Wang, S., Zhao, Y., Sun, Y., Wang, W., Chen, J., & Zhang, Y. (2022). Design of a Differential Low-Noise Amplifier Using the JFET IF3602 to Improve TEM Receiver. *Micromachines*, *13*(12), 2211.

Wang, X., Wang, D., He, J., & Takagi, N. (2021). Characteristics of Electric Currents in Upward Lightning Flashes From a Windmill and its Lightning Protection Tower in Japan, 2005–2016. *Journal of Geophysical Research: Atmospheres*, *126*(8), e2020JD034346.

Wang, Z., Deng, M., Chen, K., Wang, M., Zhang, Q., & Zeng, D. (2014). Development and evaluation of an ultralow-noise sensor system for marine electric field measurements. *Sensors and Actuators A: Physical*, *213*, 70–78.

Warner, E. H., & Kunz, J. (1919). *Corona discharge*. University of Illinois at Urbana Champaign, College of Engineering ….

Waters, R. T. (1977). *Positive discharges in long air gaps at Les Renardières*. https://api.semanticscholar.org/CorpusID:125967477

Weber, M. G., & Stocks, B. J. (1998). Forest fires and sustainability in the boreal forests of Canada. *Ambio*, *27*(7), 545–550.

Williams, A. B., & Taylor, F. J. (2006). *Electronic filter design handbook*. McGraw-Hill Education.

Wu, T., Wang, D., Rison, W., Thomas, R. J., Edens, H. E., Takagi, N., & Krehbiel, P. R. (2017). Corona discharges from a windmill and its lightning protection tower in winter thunderstorms. *Journal of Geophysical Research: Atmospheres*, *122*(9), 4849–4865.

Yang, J., Qie, X., Zhang, G., & Wang, H. (2008). Magnetic field measuring system and current retrieval in artificially triggering lightning experiment. *Radio Science*, *43*(02), 1–6.

Yang, Y., Qiu, Z., Qin, Z., Chen, M., & Du, Y. (2018). *Preliminary results of lightning current measurements at the 356 m high Shenzhen Meteorological Gradient Tower in South China*. 1–4.

Yun, C.-M., Kim, D.-Y., Choi, Y.-I., & Han, M.-K. (1995). A monolithic current limiting power MOSFET. *Proceedings of 1995 International Conference on Power Electronics and Drive Systems. PEDS 95*, 71–74.

Z. Qiu, Y. Yang, Z. Qin, M. Chen, F. Lyu, H. Guo, Y. Du, Y. Gao, G. Zhang, & S. Wang. (2019). Optical and Current Measurements of Lightning Attachment to the 356-m-High Shenzhen Meteorological Gradient Tower in Southern Coastal Area of China. *IEEE Access*, *7*, 155372–155380. https://doi.org/10.1109/ACCESS.2019.2949127

Zhang, Y., Krehbiel, P. R., Zhang, Y., Lu, W., Zheng, D., Xu, L., & Huang, Z. (2017). Observations of the initial stage of a rocket-and-wire-triggered lightning discharge. *Geophysical Research Letters*, *44*(9), 4332–4340.

Zhang, Y., Yang, S., Lu, W., Zheng, D., Dong, W., Li, B., Chen, S., Zhang, Y., & Chen, L. (2014). Experiments of artificially triggered lightning and its application in Conghua, Guangdong, China. *Atmospheric Research*, *135*, 330–343.

Zhang, Y., Zhang, Y., Xie, M., Zheng, D., Lu, W., Chen, S., & Yan, X. (2016). Characteristics and correlation of return stroke, M component and continuing current for triggered lightning. *Electric Power Systems Research*, *139*, 10–15.

Zhou, H., Theethayi, N., Diendorfer, G., Thottappillil, R., & Rakov, V. (2009). *A new approach to estimation of effective height of towers on mountain tops for lightning incidence studies: Sensitivity analysis*. X International Symposium on Lightning Protection (SIPDA), Curitiba, Brazil.